This is the accepted version of the work. The final published article is available at https://doi.org/10.1139/cgj-2025-0133.

Title Page

Manuscript ID: cgj-2025-0133

Article title:

Insights into 3D particle crushing under dynamic conditions using an improved variable bond force peridynamic model

Author information:

Luyu WANG, Postdoctoral fellow
Department of Civil and Environmental Engineering, The Hong Kong Polytechnic University, Hung Hom, Kowloon, Hong Kong SAR, China
Institute of Rock and Soil Mechanics, Chinese Academy of Sciences, 430071 Wuhan, China
E-mail: luyu.wang@polyu.edu.hk; luyu.wang@hotmail.com
ORCID: https://orcid.org/0000-0003-2882-3503
Zhen-Yu YIN, Professor (*Corresponding author)
Department of Civil and Environmental Engineering, The Hong Kong Polytechnic University, Hung Hom, Kowloon, Hong Kong SAR, China
E-mail: zhenyu.yin@polyu.edu.hk
Web: http://geoinvention.com/rteam_yinzhenyu.html
ORCID: https://orcid.org/0000-0003-4154-7304
Weizhong CHEN, Professor
Institute of Rock and Soil Mechanics, Chinese Academy of Sciences, 430071 Wuhan, China
E-mail: wzchen@whrsm.ac.cn
Webpage: https://www.sciencedirect.com/author/57222426475/weizhong-chen

Article word count:

Total word count: within 10700
Word count of Abstract: 173
Figures: 18
Tables: 2

Revised manuscript (Clean version)

Insights into 3D particle crushing under dynamic conditions using an improved variable bond force peridynamic model

Luyu Wang[a,b], Zhen-Yu Yin*[b], Weizhong Chen[a]

[a] *State Key Laboratory of Geomechanics and Geotechnical Engineering Safety, Institute of Rock and Soil Mechanics, Chinese Academy of Sciences, 430071 Wuhan, China*

[b] *Department of Civil and Environmental Engineering, The Hong Kong Polytechnic University, Hung Hom, Kowloon, Hong Kong, China*

***Corresponding author** (Prof. Z-Y Yin)

E-mail addresses: luyu.wang@polyu.edu.hk (L Wang, Postdoctoral fellow); zhenyu.yin@polyu.edu.hk (Z-Y Yin, Professor); wzchen@whrsm.ac.cn (W Chen, Professor)

Abstract: Simulation of particle crushing is a critical topic in computational mechanics, and in particular, 3D dynamic damage analysis using peridynamics (PD) constitutes an attractive research field. This study proposes a variable bond force peridynamic model (VBF-PD) that incorporates 3D micromodulus functions for different VBF forms, which have not been presented in previous literature. The proposed VBF-PD is capable of capturing the variation of bond force density along the interaction direction of a PD bond. An improved dynamic damage model is developed to effectively simulate particle crushing. Two constraint methods are introduced to characterise the interactions of deformable particle-particle and rigid impactor-particle. Then, benchmark tests are performed to examine numerical performance of the proposed VBF-PD. The results demonstrate that the method effectively simulates particle crushing with high fidelity. The particle aggregation model is constructed to explore the effects of particle arrangements, loadings, and material properties on failure modes. The findings provide valuable insights, revealing that the behaviour of particle aggregations differs significantly from that of few-particle systems due to the complex interactions among particles.

Keywords: particle crushing; breakage; granular material; peridynamics; dynamic loading; three-dimensional modelling

---

Highlights:

- A variable bond force peridynamic model (VBF-PD) is proposed for modelling 3D particle crushing during dynamic impact processes.
- An improved dynamic damage model is developed to describe crushing of particle aggregation involving multiple particles.
- Efficient constraint methods are proposed for addressing interactions of particle-particle and impactor-particle.
- Effects of particle arrangements, loadings, and material properties on dynamic damage of particle aggregations are thoroughly explored.

---

1. Introduction

Particle crushing is a fundamental phenomenon in granular mechanics, critical for understanding mechanical properties and material stability, as it reveals the macroscopic mechanisms of geomaterial breakage. Breakage of particle systems alters the morphology of particle distributions and the interparticle contact states within particle aggregations (Einav 2007a, 2007b). These effects further modify the mechanical and hydraulic properties of granular aggregations, including strength, stiffness, and permeability (de Gennes 1998; Mesri and Vardhanabhuti 2009; Zhao et al. 2023). The macroscopic stability of structures, such as foundations, excavations, and slopes, is fundamentally influenced by progressive damage at the small scale (Chen et al. 2021; Zar et al. 2024), and is also affected by the mechanical properties of the aggregate materials (Rui et al. 2020; Tan et al. 2021). Therefore, studying breakage and damage mechanisms enables engineers to predict material behaviour under complex environments, design safer structures, and optimize performance in infrastructure projects (Ogata and Yasuhara 2023; Zar et al. 2024). Many research works have been dedicated to this topic, including theoretical analysis (Henkes and Chakraborty 2009; Buscarnera and Einav 2021), experiments (Hall and Wright 2015; Tang et al. 2022; Li et al. 2024), and numerical simulations (Einav 2007b; Augarde et al. 2021). Nevertheless, several key challenges persist, as outlined below: (1) Particle interactions: unlike continuous media, granular materials exhibit intricate behaviours influenced by factors such as particle size, arrangement modes, and material properties (de Gennes 1998; Zhao et al. 2023); (2) Dynamic characteristics: failure mechanisms involve intricate damage and dynamic responses, which make failure prediction particularly difficult (Einav 2007a, 2007b); and (3) Nonlinear effects: impact loading introduces nonlinearities that further complicate simulation (Pöschel and Schwager 2005). To this end, this study aims to develop an efficient method for modelling the crushing of 3D particles.

Advanced computational methods are essential for capturing the complexities described above and for improving understanding of breakage mechanisms. Over the past decades, numerous efficient numerical methods have been proposed to address the challenges in particle crushing simulations (Einav 2007b; Augarde et al. 2021; Pöschel and Schwager 2005; Bui and Nguyen 2021). These methods can be basically categorized into three groups: (1) the mesh-based methods; (2) the particle-based methods; (3) the coupling methods. The Finite Element Method (FEM) (Chung and Chiang 1996; Turner et al. 2019; Zhang et al. 2020) and the Material Point Method (MPM) (Liang et al. 2024) are two representative mesh-based methods extensively applied in granular mechanics. However, both FEM and MPM require additional treatments to better capture the intricate interactions among particles. The finite element-based methods are renowned for accuracy in continuum mechanics but faces significant challenges in large deformations and discontinuities (Jin et al. 2021; Wong and Cui 2023). Issues such as severe mesh distortion and remeshing hinder its ability to accurately model large deformations and failure. MPM combines particle- and mesh-based approaches, addressing some issues in FEM but additionally introduces its own tough nuts. The transfer of information between particles and the meshes leads to numerical diffusion and inaccuracies, particularly when simulating sharp interfaces and complex interactions in granular systems (Augarde et al. 2021). The particle-based methods, such as the Discrete Element Method (DEM) (Lobo-Guerrero and Vallejo 2005; de Bono and McDowell 2020; Wang and

Yin 2022) and Smoothed Particle Hydrodynamics (SPH) (Yin et al. 2018; Longo et al. 2019), are generally more effective in handling these scenarios. The Contact Dynamics Method (CDM) (Azéma et al. 2013), grounded in rigorous contact theory, serves as a foundation for both DEM and SPH, enabling them to accurately capturing contact mechanics. DEM excels in capturing rigid particle interactions but struggles with computational efficiency when simulating large numbers of particles. Besides, it faces difficulties in accurately modelling fine-scale phenomena, especially breakage and progressive failure processes. SPH is well-suited for handling fluid-like behaviours and large deformations but suffers from numerical instability and inaccuracies in capturing contact forces. The CDM, DEM and SPH require substantial computational resources and may face issues in achieving high-resolution simulations for the detailed damage analysis.

On the other hand, many advanced techniques have been developed by coupling different numerical frameworks, typically the Finite Element-Discrete Element Method (FEM-DEM) (Li et al. 2016; Ma et al. 2016; Wei et al. 2019), the Phase-Field-DEM (PF-DEM) (Sac-Morane et al. 2024), the Computational Fluid Dynamics-DEM (CFD-DEM) (Liu et al. 2020; Wang et al. 2025), and the Particle Finite Element Method (PFEM) (Jin et al. 2021). However, FEM-DEM and PF-DEM often face challenges with computational efficiency due to the complexity in integrating the continuum (FEM or PF) and discrete (DEM) components. The interface between these components can lead to inaccuracies and make it difficult to capture fine-scale interactions and damage. CFD-DEM may encounter difficulties in modelling damage progression and finer details of particle crushing (Augarde et al. 2021; Bui and Nguyen 2021). PFEM has achieved great success in modelling large deformations and failure of solids, particularly in geotechnical stability problems (Jin et al. 2021). As a finite element-based method, it lacks the capability in capturing granular material breakage. Therefore, it is essential to develop a new framework to address the limitations of conventional methods.

Given this challenge, the nonlocal theory provides an effective solution. Peridynamic (PD) theory, pioneered by Silling (Silling 2000; Silling et al. 2007), is a nonlocal framework successfully used to model spontaneous damage. In contrast to conventional methods, PD formulates the governing equation as an integral-differential form, facilitating damage simulations without additional techniques (Silling and Lehoucq 2010). Damage simulation is achieved by eliminating bond interactions between PD particles, thereby representing damage evolution within a unified framework. The original PD formulation proposed by Silling (2000), known as the bond-based PD (BB-PD). One advantage of PD framework is that it eliminates the need to calculate the stress intensity factor, as required in classical fracture mechanics (Bobaru et al. 2016; Wang et al. 2024a). But it is constrained by a fixed Poisson's ratio, limiting its ability to model material incompressibility. To overcome these drawbacks, the ordinary state-based peridynamics (OSB-PD) and the non-ordinary state-based peridynamics (NOSB-PD) have been proposed (Silling et al. 2007; Silling and Lehoucq 2010; Madenci and Oterkus 2013). These achievements improve flexibility and accuracy of PD in capturing complex material behaviours (Bobaru et al. 2016; Wang et al. 2023; Wang and Yin 2024b) as well as coupling process (Bie et al. 2024a, 2024b). In this study, we focus on brittle and elastic granular materials without delving into complex material constitutive relations. We aim to modify the BB-PD framework to enhance its applicability for 3D particle breakage.

Although some studies have focused on simulating particle crushing using PD, most have focused on the analysis of single particles, as seen in works such as (Blanc et al. 2021; Diehl et al. 2019; Walayat et al. 2023). In PD simulation, a single particle is usually impacted by a rigid object to replicate particle breakage under rigid body impact conditions. Nevertheless, modelling interactions among multiple particles remains challenging (Pöschel and Schwager 2005; Augarde et al. 2021; Bui and Nguyen 2021). A key issue is the need to integrate the DEM-based algorithms to update the contact forces between particles (Wang et al. 2023; Neto 2023). However, this treatment is often impractical due to the substantial computational resources required for detecting contact interfaces (Neto 2023). Even if the contact interfaces can be accurately detected, achieving reliable numerical convergence continues to pose a major challenge (Konrad and Salami 2018; Wang et al. 2022). Based on the challenges outlined above, this study focuses on the following aspects: (1) developing an improved variable bond force peridynamic framework (VBF-PD); (2) integrating an improved dynamic damage model into the proposed framework; (3) proposing constraint methods for particle interactions; and (4) exploring the mechanisms of particle crushing during impact contact.

The article is organised as follows. Section 2 provides the fundamental formulation of PD. Section 3 proposes the VBF-PD with integration of an improved dynamic damage model. It includes the derivations of 3D VBF, which have not been presented in existing literature. Section 4 discusses modelling methods for particle-particle and impactor-particle interactions. Sections 5 and 6 provide details on numerical discretisation, validations, and applications.

2. Fundamental formulation of peridynamics

2.1 Peridynamic kinematics

As shown in Fig. 1, a solid medium occupies a space in the reference (initial) configuration Ω_0, and evolves into the current configuration under deformation, denoted as Ω_t. A material point within Ω_0 is denoted by $\boldsymbol{x}$, which interacts with neighbouring points $\boldsymbol{x}'$ within a range defined by the peridynamic horizon δ. In PD formulation, the peridynamic bond, defined as $\boldsymbol{\xi} = \boldsymbol{x}' - \boldsymbol{x}$, is introduced to capture the relative position between material points $\boldsymbol{x}$ and $\boldsymbol{x}'$ (Silling 2000). The length of a bond is expressed as $|\boldsymbol{\xi}|$. The relation $|\boldsymbol{\xi}| < \delta$ defines the set of neighbouring points associated with $\boldsymbol{x}$. The peridynamic family of point $\boldsymbol{x}$ is represented by $H_x = \{\boldsymbol{x}' | \boldsymbol{x} \in \Omega_0, \boldsymbol{x}' \in \Omega_0, |\boldsymbol{x}' - \boldsymbol{x}| < \delta\}$ (Silling and Lehoucq 2010; Wang and Yin 2024b).

During deformation or failure of the solid medium, the positions of material points $\boldsymbol{x}$ and $\boldsymbol{x}'$ are transformed to $\boldsymbol{y}$ and $\boldsymbol{y}'$, respectively. The displacements $\boldsymbol{u}$ and $\boldsymbol{u}'$ corresponding to these two points are represented by:

$$\begin{aligned} \boldsymbol{u} &= \boldsymbol{u}(\boldsymbol{x},t) = \boldsymbol{y} - \boldsymbol{x} \\ \boldsymbol{u}' &= \boldsymbol{u}(\boldsymbol{x}',t) = \boldsymbol{y}' - \boldsymbol{x}' \end{aligned} \tag{1}$$

where t represents time. The relative displacement $\boldsymbol{\eta}$ (the current bond) between material points is calculated by:

$$\boldsymbol{\eta} = \boldsymbol{u}' - \boldsymbol{u} = (\boldsymbol{y}' - \boldsymbol{y}) - \boldsymbol{\xi} \tag{2}$$

which indicates that the bond $\boldsymbol{\xi}$ is represented as $\boldsymbol{\eta} + \boldsymbol{\xi}$ in the current configuration, as illustrated in Fig. 1. The bond stretch, denoted by s, characterises the relative variation in the length of bond $\boldsymbol{\xi}$ and is calculated by:

$$s = \frac{|\boldsymbol{\eta} + \boldsymbol{\xi}| - |\boldsymbol{\xi}|}{|\boldsymbol{\xi}|} \tag{3}$$

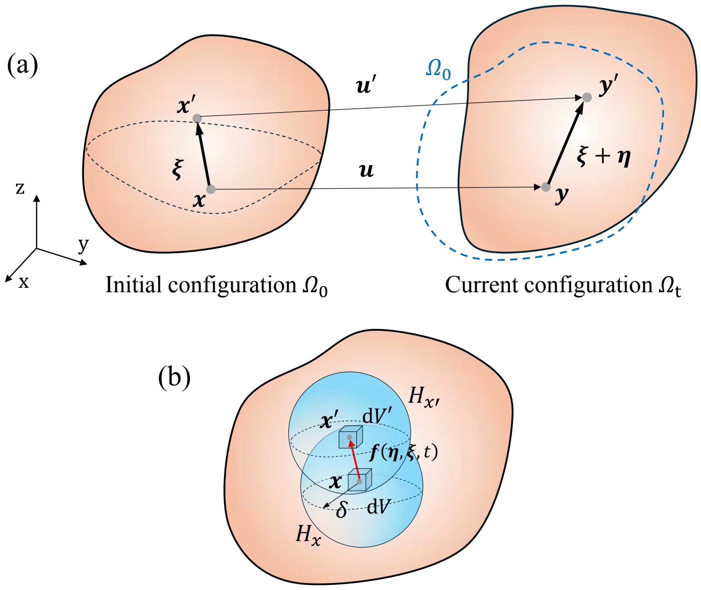

Fig. 1. Schematic of peridynamic model: (a) The initial and current configurations; (b) Peridynamic material points.

In PD, the interaction between any pair of two material points is described by the pairwise bond force density function $\boldsymbol{f}$ (Silling and Lehoucq 2010; Wang and Yin 2024b). The function $\boldsymbol{f}(\boldsymbol{\eta},\boldsymbol{\xi},t)$ represents the force (unit: per unit volume squared) exerted by point $\boldsymbol{x}'$ on point $\boldsymbol{x}$, while $-\boldsymbol{f}(\boldsymbol{\eta},\boldsymbol{\xi},t)$ represents the force exerted by point $\boldsymbol{x}$ on point $\boldsymbol{x}'$. Therefore, the internal force within the solid medium can be captured by function $\boldsymbol{f}$.

The peridynamic momentum balance equation of point $\boldsymbol{x}$ is formulated as follows (Silling and Lehoucq 2010; Wang et al. 2023):

$$\rho\ddot{\boldsymbol{u}}(\boldsymbol{x},t) = \boldsymbol{L}(\boldsymbol{x},t) + \boldsymbol{b}(\boldsymbol{x},t) \tag{4}$$

where $\ddot{\boldsymbol{u}}(\boldsymbol{x},t)$ represents the acceleration of point $\boldsymbol{x}$, ρ is the mass density in the reference configuration, $\boldsymbol{b}(\boldsymbol{x},t)$ denotes the body force density vector. The internal force function $\boldsymbol{L}(\boldsymbol{x},t)$ (unit: per unit volume) is formulated as (Silling and Lehoucq 2010; Wang and Yin 2024b):

$$\boldsymbol{L}(\boldsymbol{x},t) = \nabla \cdot \boldsymbol{\sigma}(\boldsymbol{x},t) = \int_{H_x} \boldsymbol{f}(\boldsymbol{\eta},\boldsymbol{\xi},t)\,\mathrm{d}V' \tag{5}$$

where $\mathrm{d}V'$ denotes the infinitesimal volume associated with $\boldsymbol{x}'$. This treatment eliminates the necessity for derivative calculations inherent in classical elasticity, replacing the divergence of the stress tensor, $\nabla \cdot \boldsymbol{\sigma}(\boldsymbol{x},t)$, with an integral form. The function $\boldsymbol{f}(\boldsymbol{\eta},\boldsymbol{\xi},t)$ must satisfy the admissibility conditions (Silling 2000; Silling et al. 2007), which are expressed through the conservations of linear and angular momentum, $\boldsymbol{f}(-\boldsymbol{\eta},-\boldsymbol{\xi},t) = -\boldsymbol{f}(\boldsymbol{\eta},\boldsymbol{\xi},t)$ and $(\boldsymbol{\eta}+\boldsymbol{\xi})\times\boldsymbol{f}(\boldsymbol{\eta},\boldsymbol{\xi},t)=0$.

2.2 Constitutive relations in peridynamics

In this study, we use the well-developed constitutive modelling method proposed by Silling and Askari (2005) and Silling and Lehoucq (2010), known as the microelastic material model. This model requires that the condition $\int_{\Gamma}\boldsymbol{f}(\boldsymbol{\eta},\boldsymbol{\xi},t)\mathrm{d}\boldsymbol{\eta}=0$ be satisfied, where Γ is an arbitrary closed path within the medium. It implies that the pairwise bond force density $\boldsymbol{f}$ can be derived from a potential function $w(\boldsymbol{\eta},\boldsymbol{\xi})$ (unit: per energy unit volume squared), formulated as (Silling 2000; Silling and Askari 2005):

$$\boldsymbol{f}(\boldsymbol{\eta},\boldsymbol{\xi},t)=\frac{\partial w(\boldsymbol{\eta},\boldsymbol{\xi})}{\partial\boldsymbol{\eta}} \tag{6}$$

Consequently, the energy density (unit: per unit volume), denoted as e, can be calculated by:

$$e=\frac{1}{2}\int_{H_x} w(\boldsymbol{\eta},\boldsymbol{\xi})\,\mathrm{d}V_{\xi} \tag{7}$$

where $\mathrm{d}V_{\xi}$ represents the volume associated with $\boldsymbol{x}$. The potential function $w(\boldsymbol{\eta},\boldsymbol{\xi})$ determines the complete forms of the bond force density $\boldsymbol{f}$ and the energy density e. An implicit representation of the force density function can be derived from Eqs. (6) and (7) as follows:

$$\boldsymbol{f}(\boldsymbol{\eta},\boldsymbol{\xi},t)=F(|\boldsymbol{\eta}+\boldsymbol{\xi}|,\boldsymbol{\xi})\frac{\boldsymbol{\eta}+\boldsymbol{\xi}}{|\boldsymbol{\eta}+\boldsymbol{\xi}|} \tag{8}$$

where $F(|\boldsymbol{\eta}+\boldsymbol{\xi}|,\boldsymbol{\xi})$ is a scalar function that exclusively depends on the length of current bond $\boldsymbol{\eta}+\boldsymbol{\xi}$ and the initial bond vector $\boldsymbol{\xi}$ (Silling and Askari 2005; Wang and Yin 2025). The prototype microelastic brittle (PMB) model offers a widely used form for the function F:

$$F(|\boldsymbol{\eta}+\boldsymbol{\xi}|,\boldsymbol{\xi})=cs\mu(\boldsymbol{\xi},t) \tag{9}$$

where c is the micromodulus function of the PMB material, s is the bond stretch (Eq. (3)), and $\mu(\boldsymbol{\xi},t)$ is the damage indicator. The expression of c is derived based on the equivalence between the energy density calculated by classical elasticity and peridynamics, given by Silling and Askari (2005) and Madenci and Oterkus (2013):

$$c=\begin{cases}\dfrac{18K}{\pi\delta^4}, & \text{for 3D}\\[2ex] \dfrac{12K'}{\pi h\delta^3}, & \text{for 2D}\end{cases} \tag{10}$$

where K and h represent the bulk modulus and thickness of material, respectively. The 2D bulk modulus K' is given by $K'=E/(2(1-\nu))$ for plane stress problem and $K'=E/(2(1+\nu)(1-2\nu))$ for plane strain, where E and ν denote Young's modulus and Poisson's ratio.

Consistent with the relevant works (Silling 2000; Wang and Yin 2025), our result Eq. (8) can be recast into:

$$\boldsymbol{f}(\boldsymbol{\eta},\boldsymbol{\xi},t) = \boldsymbol{C}(\boldsymbol{\xi})\boldsymbol{\eta} \quad \text{for any } \boldsymbol{\xi} \text{ and } \boldsymbol{\eta} \tag{11}$$

where $\boldsymbol{C}(\boldsymbol{\xi})$ is the micromodulus tensor, generally written as $\boldsymbol{C}(\boldsymbol{\xi}) = \partial\boldsymbol{f}(\boldsymbol{0},\boldsymbol{\xi})/\partial\boldsymbol{\eta}$, and it satisfies the symmetry condition $\boldsymbol{C}(-\boldsymbol{\xi}) = \boldsymbol{C}(\boldsymbol{\xi})$ for any $\boldsymbol{\xi}$ (Wang and Yin 2025). On the other hand, from Eqs. (8) and (9), and substituting Eq. (3), the micromodulus tensor for a linearized model can be obtained:

$$\boldsymbol{C}(\boldsymbol{\xi}) = \frac{c\mu(\boldsymbol{\xi},t)}{|\boldsymbol{\xi}|}\frac{\boldsymbol{\eta}+\boldsymbol{\xi}}{|\boldsymbol{\eta}+\boldsymbol{\xi}|} \otimes \frac{\boldsymbol{\eta}+\boldsymbol{\xi}}{|\boldsymbol{\eta}+\boldsymbol{\xi}|} \tag{12}$$

The method for determining $\mu(\boldsymbol{\xi},t)$ in Eqs. (9) and (12) and the details of peridynamic damage modelling will be elaborated in Section 3.3.

3. The variable bond force peridynamic model (VBF-PD)

In this section, a 3D variable bond force peridynamic (VBF-PD) model is proposed, incorporating different VBF types for the construction of micromodulus functions. Then, an improved damage model is proposed to simulate the variable critical bond strain and mixed failure modes.

3.1 Conventional bond force function

The conventional form of bond force density function is derived from the linearized formulation of bond-based peridynamics (Silling and Askari 2005). Combining Eqs. (8) and (9), it yields:

$$\boldsymbol{f}(\boldsymbol{\eta},\boldsymbol{\xi},t) = sc\mu(\boldsymbol{\xi},t)\frac{\boldsymbol{\eta}+\boldsymbol{\xi}}{|\boldsymbol{\eta}+\boldsymbol{\xi}|} \tag{13}$$

The conventional form of the micromodulus function c used in Eq. (13) remains constant along the peridynamic bond $\boldsymbol{\xi}$, resulting in a fixed value of $\boldsymbol{f}(\boldsymbol{\eta},\boldsymbol{\xi},t)$ during solid deformation, as illustrated in Fig. 2a. However, from a physical perspective, the value of material parameter c should depend on the length of bond, denoted as $|\boldsymbol{\xi}|$. Notably, Kilic and Madenci (2009), Huang et al. (2015a), and Wang and Yin (2025) have proposed various approaches to account for the variation in c.

Previous studies have explored the effect of different forms of c in PD simulations (Kilic and Madenci 2009; Huang et al. 2015a; Li et al. 2021), but limited results have presented for variable c in 3D formulations. Herein, we revise the conventional bond force function (Eq. (13)) by rearranging c as a function of the peridynamic bond $\boldsymbol{\xi}$:

$$c(\boldsymbol{\xi}) = c_0 g(\boldsymbol{\xi}) \tag{14}$$

where $g(\boldsymbol{\xi})$ represents the attenuation function. In the conventional bond force form (Eq. (13)), $g(\boldsymbol{\xi}) = 1$, and the initial micromodulus c_0 is determined by Eq. (10), which remains constant once the horizon δ is specified. Then, we derive the explicit form of variable $g(\boldsymbol{\xi})$ in the following section.

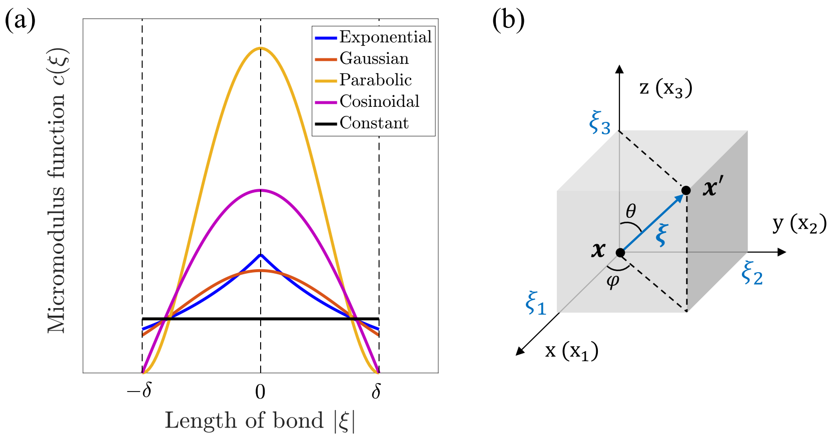

Fig. 2. Illustration of VBF: (a) Variation of $c(\boldsymbol{\xi})$ with change of distance $|\boldsymbol{\xi}|$; (b) The relative positions between two PD points in the spherical coordinate system.

3.2 The variable bond force (VBF) function

According to Eqs. (13) and (14), the improved version of the bond force function (the VBF function) can be written as:

$$\boldsymbol{f}(\boldsymbol{\eta},\boldsymbol{\xi},t) = sc_0 g(\boldsymbol{\xi})\mu(\boldsymbol{\xi},t)\frac{\boldsymbol{\eta}+\boldsymbol{\xi}}{|\boldsymbol{\eta}+\boldsymbol{\xi}|} \tag{15}$$

Correspondingly, the expression of the micromodulus tensor (Eq. (12)) can be recast into:

$$\boldsymbol{C}(\boldsymbol{\xi}) = c_0 g(\boldsymbol{\xi})\frac{\mu(\boldsymbol{\xi},t)}{|\boldsymbol{\xi}|}\frac{\boldsymbol{\eta}+\boldsymbol{\xi}}{|\boldsymbol{\eta}+\boldsymbol{\xi}|}\otimes\frac{\boldsymbol{\eta}+\boldsymbol{\xi}}{|\boldsymbol{\eta}+\boldsymbol{\xi}|} \tag{16}$$

where the method for determining $g(\boldsymbol{\xi})$ is crucial for achieving variable bond forces in the VBF-PD. To this end, we introduce the criteria for constructing the attenuation function $g(\boldsymbol{\xi})$, also referred to as the kernel function, which are expressed as follows (Huang et al. 2015a; Wang and Yin 2025):

$$\begin{cases} g(\boldsymbol{\xi}) = g(-\boldsymbol{\xi}) \\ \lim\limits_{|\boldsymbol{\xi}|\to 0} g(\boldsymbol{\xi}) = \max g \\ \lim\limits_{|\boldsymbol{\xi}|\to \delta} g(\boldsymbol{\xi}) = 0 \\ \int_{-\infty}^{\infty} \lim\limits_{\delta\to 0} g(\boldsymbol{\xi}) = 1 \end{cases} \tag{17}$$

In the VBF-PD, the expression of c_0 differs from that in the conventional bond force form. Most of the relevant literature provides the expressions of c_0 only under 1D or 2D conditions (Huang et al. 2015a; Wang and Yin 2025). In this study, we extend these results to 3D conditions. The derivation procedure is analogous to that of Silling and Askari (2005) and Madenci and Oterkus (2013), where the strain energy densities calculated from classical continuum mechanics (W^{CM}) and peridynamics (W^{PD}) are equated. In the spherical coordinate system $O(\varphi,\theta,|\boldsymbol{\xi}|)$ illustrated in Fig. 2b, W^{PD} is computed by:

$$W^{\mathrm{PD}} = \frac{1}{2}\int_0^{\delta}\int_0^{2\pi}\int_0^{\pi}\left(c_0 g(\boldsymbol{\xi})\frac{s_0^2|\boldsymbol{\xi}|^3}{2}\sin\varphi\right)\mathrm{d}\varphi\,\mathrm{d}\theta\,\mathrm{d}|\boldsymbol{\xi}| \tag{18}$$

where φ and θ are azimuth and polar angles, respectively. s_0 is the bulk stretch in dilatant deformation. The specified forms of $g(\boldsymbol{\xi})$ can be chosen in different forms (Li et al. 2021). In this study, we consider five types, as listed in Table 1.

Table 1

Expressions of different VBF functions and the corresponding quantities derived in this study.

Function form	$g(\boldsymbol{\xi})$	c_0	W^{PD}	W^{CM}
Exponential VBF	$\mathrm{e}^{-\frac{\lvert\boldsymbol{\xi}\rvert}{\delta}}$	$\frac{3}{\left(12-\frac{32}{\mathrm{e}}\right)}\frac{E}{(1-2\nu)\delta^4\pi}$	$\pi c_0\delta^4 s_0^2\left(6-\frac{16}{\mathrm{e}}\right)$	$\frac{3}{2}\frac{E}{(1-2\nu)}s_0^2$ for all VBF forms
Gaussian VBF	$\mathrm{e}^{-\left(\frac{\xi}{\delta}\right)^2}$	$\frac{3}{\left(1-\frac{2}{\mathrm{e}}\right)}\frac{E}{(1-2\nu)\delta^4\pi}$	$\pi c_0\delta^4 s_0^2\left(\frac{1}{2}-\frac{1}{\mathrm{e}}\right)$	
Parabolic VBF	$\left(1-\left(\frac{\boldsymbol{\xi}}{\delta}\right)^2\right)^2$	$\frac{36E}{(1-2\nu)\delta^4\pi}$	$\frac{\pi c_0\delta^4 s_0^2}{24}$	
Cosinoidal VBF	$\cos\frac{\pi\boldsymbol{\xi}}{2\delta}$	$\frac{3\pi^4}{4(\pi^3-24\pi+48)}\frac{E}{(1-2\nu)\pi\delta^4}$	$\frac{2}{\pi^3}c_0\delta^4 s_0^2(\pi^3-24\pi+48)$	
Constant VBF	1	$\frac{6E}{(1-2\nu)\delta^4\pi}$	$\frac{\pi c_0\delta^4 s_0^2}{4}$	

Remarks: (1) $g(\boldsymbol{\xi})$ is the attenuation function. c_0 is the initial micromodulus. W^{CM} and W^{PD} are the strain energy densities in continuum mechanics and peridynamics. (2) $g(\boldsymbol{\xi})=1$ corresponds to the constant function used in the conventional formulation. (3) The derivation details are provided in Appendix A.

By Analogy with Eq. (18), the strain energy density W^{CM} in classical continuum mechanics (Malvern 1969) is computed under the same loading conditions as in the derivation of W^{PD}:

$$W^{\mathrm{CM}} = \frac{1}{2}\lambda(\varepsilon_{kk}\varepsilon_{kk})^2 + \mu\varepsilon_{ij}\varepsilon_{ij} \tag{19}$$

where ε_{ij} are the components of strain tensor, ε_{kk} are the principal components of strain tensor, λ_{L} and μ_{L} are the Lamé elastic constants, given by $\lambda_{\mathrm{L}} = E\nu/((1+\nu)(1+2\nu))$ and $\mu_{\mathrm{L}} = E/(2(1+\nu))$. Substituting $g(\boldsymbol{\xi})$ from Table 1 into Eq. (18) and combining it with Eq. (19), different forms of c_0 under 3D conditions are obtained by relation $W^{\mathrm{CM}} = W^{\mathrm{PD}}$. The results are summarised in Table 1, with detailed derivations provided in Appendix A.

Fig. 2a illustrates the variation of $c(\boldsymbol{\xi})$ (Eq. (14)) with varying $\boldsymbol{\xi}$. The properties of different forms of $c(\boldsymbol{\xi})$ are summarised as follows:

- The constant VBF used in the conventional method fails to capture variation in $c(\boldsymbol{\xi})$.
- The parabolic VBF achieves the relatively highest value; the exponential type exhibits a sharp discontinuity at the position of PD point itself (at $|\boldsymbol{\xi}| = 0$).
- The values of parabolic and cosinoidal types are zero at the edge of horizon δ (at $|\boldsymbol{\xi}| = \delta$).
- From Table 1, there are no substantial differences among the various forms of VBF. The main distinction is that additional effort is required to calculate $\boldsymbol{\xi}$, which is not needed in the conventional

method (i.e. the constant VBF).

3.3 An improved damage model

Characterisation of damage. In PD, material damage is described by the breakage of bonds between material points. The critical bond strain s_{c} is a core parameter in damage simulations. It is determined by equating the energy release rate calculated from classical elasticity with that from peridynamics, expressed as (Madenci and Oterkus 2013; Wang et al. 2023):

$$s_{\mathrm{c}} = \begin{cases} \sqrt{\dfrac{5G_{\mathrm{c}}}{9K\delta'}} & \text{for 3D} \\[2em] \sqrt{\dfrac{\pi G_{\mathrm{c}}}{3K'\delta'}} & \text{for 2D} \end{cases} \tag{20}$$

where G_{c} represents a material property obtained from fracture mechanics experiments, commonly referred to as the critical energy release rate (Silling and Askari 2005; Wang et al. 2023). The damage indicator $\mu(\boldsymbol{\xi},t)$ introduced in Eqs. (9) and (12) depends on s_c. For tensile-sensitive damage (T-D) materials, $\mu(\boldsymbol{\xi},t)$ can be determined based on the value of s_c as follows:

$$\mu(\boldsymbol{\xi},t) = \begin{cases} 1, & \text{if } s < s_{\mathrm{c}} \\ 0, & \text{if } s \geq s_{\mathrm{c}} \end{cases}, \quad \text{for T-D} \tag{21}$$

Then, once $\mu(\boldsymbol{\xi},t)$ for each peridynamic bond is obtained, the local damage factor $d(\boldsymbol{x},t)$ associated with point $\boldsymbol{x}$, as well as the global damage factor D_{g} of the solid medium, can be calculated as follows:

$$\begin{aligned} d(\boldsymbol{x},t) &= \frac{\int_{H_x} \left(1 - \mu(\boldsymbol{\xi},t)\right) \mathrm{d}V_{\xi}}{\int_{H_x} \mathrm{d}V_{\xi}} \\ D_{\mathrm{g}} &= \frac{N_{\mathrm{fail}}}{N_{\mathrm{total}}} \end{aligned} \tag{22}$$

where N_{fail} and N_{total} denote the numbers of broken bonds and total bonds, respectively.

Compression and tensile failure mode. In conventional PD simulations, the failure mode is typically assumed to be tensile-dominant and not sensitive to compressive loading. However, previous studies have demonstrated that brittle materials, such as concretes, rocks, and ceramics, are fragile when pre-existing defects are present (Bažant and Planas 1998). To simulate this feature, we consider the tensile-sensitive damage (T-D) criterion, and the mixed tensile and compressive-sensitive damage (TC-D) criterion.

The T-D criterion is outlined in Eq. (21), while the TC-D criterion can be defined by considering the absolute value of the bond stretch, denoted as $|s|$, written as:

$$|s| = \left|\frac{|\boldsymbol{\eta}+\boldsymbol{\xi}|-|\boldsymbol{\xi}|}{|\boldsymbol{\xi}|}\right| \tag{23}$$

Analogous to Eq. (21), the TC-D criterion is formulated as follows:

$$\mu(\boldsymbol{\xi},t) = \begin{cases} 1, & \text{if } |s| < s_{\mathrm{c}} \\ 0, & \text{if } |s| \geq s_{\mathrm{c}} \end{cases}, \quad \text{for TC-D} \tag{24}$$

Variable critical bond strain. Eq. (20) provides an approach for calculating the critical bond strain s_{c}, which is typically assumed to be constant in conventional PD simulations. However, in practical scenarios, material strength may change with the progression of deformation and damage, making a constant s_{c} inadequate to capture this feature (Silling and Askari 2005). To address this issue, a modified form of the bond stretch is defined as:

$$s'_{\mathrm{c}} = s_{\mathrm{c}} - A_0 s_{\min} \tag{25}$$

where s'_{c} is the variable bond critical strain, s_{c} is the initial critical bond strain determined by Eq. (20), A_0 is a coefficient set to 0.25 (Silling and Askari 2005), and $s_{\min}$ represents the minimum value of bond stretch among all bonds.

4. Impact contact modelling method

In this section, we develop an impact contact model to simulate particle interaction during crushing processes. To achieve this, two distinct methods are utilised to separately address particle-particle and impactor-particle interactions.

4.1 Interaction relations in aggregated particles

Simulation of particle crushing during impact contact requires a specialised technique to handle the contact at the interface between two objects, serving as a supplement to the peridynamic formulation outlined in Sections 2 and 3. Without an efficient contact modelling technique, unphysical scenarios, particularly the overlapping of contacting objects, may occur (Lu et al. 2021; Wang et al. 2023).

As illustrated in Fig. 3, following conventions in computational contact mechanics (Wriggers 2006), the loading bar is referred to as the "impactor", while the particle aggregation is considered as the "target". The primary focus is on modelling the impactor-target interaction.

An initial velocity v_0 is applied to the impactor. For illustration, we consider three identical particles, denoted as Particles P1, P2, and P3, as shown in Fig. 3a. Particle P1 serves as the target, which is in direct contact with the impactor (the loading bar). The interactions between P1-P2, P2-P3, and P1-P3 differ from the target-impactor contact. To clarify this, two types of connections are involved in this model:

- **Contact constraint (C-constraint):** Impactor-to-target (impactor-P1) interaction is modelled using the C-constraint, including the computation of the contact force, as shown in Fig. 3b. The C-constraint is typically implemented through iterative methods during impact contact.

- **Tie constraint (T-constraint):** Particle-to-particle (P1-P2, P2-P3, P1-P3) interactions are modelled using the T-constraint, where the interface between two particles is represented by a merging interface, as shown in Fig. 3c. The deformation at particle interfaces is identical for two closely positioned particles, as the particles are arranged in a compact pattern with minimal space between particle pairs.

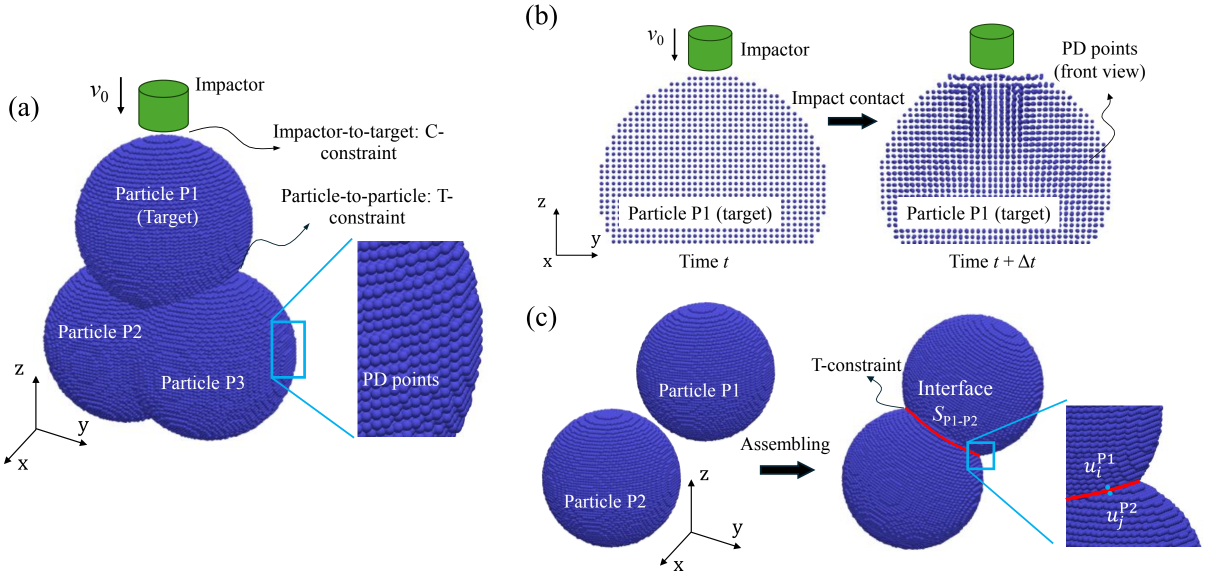

Fig. 3. Schematic of interactions in a particle system: (a) An example of simply particle system; (b) Connection of impactor-target using C-constraint; (c) Connection between two particles using T-constraint.

4.2 Impact contact algorithm

The key differences between the C- and T-constraints lie in the complexity of computing contact forces and the arrangement of material points. Further details are given as follows.

T-constraint. The interface between P1 and P2 is denoted as $S_{\text{P1-P2}}$. The displacement vectors at $S_{\text{P1-P2}}$ corresponding to P1 and P2 are represented by $\boldsymbol{u}_i^{\text{P1}}$ and $\boldsymbol{u}_j^{\text{P2}}$, as illustrated in Fig. 3c. Here, i and j denote the indices of particles at the interface. The T-constraint requires the following condition:

$$\boldsymbol{u}_i^{\text{P1}} = \boldsymbol{u}_j^{\text{P2}}, \quad \text{at } S_{\text{P1-P2}} \tag{26}$$

C-constraint. The complexity of C-constraint arises from the complexities in computing contact forces and updating particle positions. In the VBF-PD, we use the impact contact algorithm developed by Madenci and Oterkus (2013). As shown in Fig. 3b, the impactor is assumed to be rigid. The k-th PD material point at the impactor-target interface is denoted as $\boldsymbol{x}_k$. The displacements of point $\boldsymbol{x}_k$ at time t and time $t+\Delta t$ are denoted as $\boldsymbol{u}_k^t$ and $\boldsymbol{u}_k^{t+\Delta t}$, respectively. Δt represents the time increment. The velocity at time $t+\Delta t$ is calculated as:

$$\boldsymbol{v}_k^{t+\Delta t} = \frac{\boldsymbol{u}_k^{t+\Delta t} - \boldsymbol{u}_k^t}{\Delta t} \tag{27}$$

The force exerted on the impactor by point $\boldsymbol{x}_k$ is calculated by:

$$\boldsymbol{F}_k^{t+\Delta t} = -\rho_k \frac{\boldsymbol{v}_k^{t+\Delta t} - \boldsymbol{v}_k^t}{\Delta t} V_k \tag{28}$$

where ρ_k and V_k are the density and volume associated with point $\boldsymbol{x}_k$. The resultant force $\boldsymbol{F}_{\text{total}}^{t+\Delta t}$, referred to as the total force, acting on the impactor can be obtained by summing $\boldsymbol{F}_k^{t+\Delta t}$ over the particles that are penetrated inside the impactor, expressed by:

$$\boldsymbol{F}_{\text{total}}^{t+\Delta t} = \sum_{k=1} \boldsymbol{F}_k^{t+\Delta t} \lambda_k^{t+\Delta t} \tag{29}$$

where $\lambda_k^{t+\Delta t}$ is an indicator. It equals to 1 if the particle penetrates is inside the impactor; otherwise, it equals to 0.

5. Numerical discretization

5.1 Discretization forms and explicit time integration

The discretization method proposed by Silling and Askari (2005) has found extensive applications in numerical implementation of peridynamics. In this method, there are no need for connectivity information of grids or material points, making it inherently mesh-free. The integral form of the peridynamic momentum balance equation (Eq. (4)) at time step n can be discretized as:

$$\rho \ddot{\boldsymbol{u}}_i^n = \sum_{j \in H_i} \boldsymbol{f}\left(\boldsymbol{\eta}_{ji}^n, \boldsymbol{\xi}_{ji}, t\right) V_j + \boldsymbol{b}_i^n \tag{30}$$

where the variables labelled with superscript n denote the values at time step n, H_i denotes the family of PD point $\boldsymbol{x}_i$, V_j is the volume associated with $\boldsymbol{x}_j$ inside H_i, as shown in Fig. 4. $\ddot{\boldsymbol{u}}_i^n$ and $\boldsymbol{b}_i^n$ are the acceleration vector and body force density associated with $\boldsymbol{x}_i$, respectively. $\boldsymbol{\eta}_{ji}^n$ and $\boldsymbol{\xi}_{ji}$ are the current bond and the initial bond, respectively. $\boldsymbol{\eta}_{ji}^n$ depends on the displacement vectors during deformation, while $\boldsymbol{\xi}_{ji}$ is time-independent, and can be expressed as:

$$\begin{aligned} \boldsymbol{\eta}_{ji}^n &= \boldsymbol{u}_j^n - \boldsymbol{u}_i^n \\ \boldsymbol{\xi}_{ji} &= \boldsymbol{x}_j - \boldsymbol{x}_i \end{aligned} \tag{31}$$

The following simplified notations are adopted here:

$$\begin{aligned} \ddot{\boldsymbol{u}}_i^n &= \ddot{\boldsymbol{u}}(\boldsymbol{x}_i, t^n) \\ \boldsymbol{b}_i^n &= \boldsymbol{b}(\boldsymbol{x}_i, t^n) \\ \boldsymbol{f}_{ji}^n &= \boldsymbol{f}\left(\boldsymbol{\eta}_{ji}^n, \boldsymbol{\xi}_{ji}, t\right) \end{aligned} \tag{32}$$

In PD, the pairwise bond force density function $\boldsymbol{f}_{ji}^n$ can be physically interpreted as the interaction exerted on $\boldsymbol{x}_i$ by $\boldsymbol{x}_j$, whereas $\boldsymbol{f}_{ij}^n$ represents the interaction exerted on $\boldsymbol{x}_j$ by $\boldsymbol{x}_i$, as displayed in Fig. 4.

The expression of $\boldsymbol{f}_{ji}^{n}$ is given by Eq. (8) or its linearized form in Eq. (11). The discretised form of Eq. (8) is formulated as:

$$\boldsymbol{f}_{ji}^{n} = c s_{ji}^{n} \mu(\boldsymbol{\xi}_{ji}, t) \frac{\boldsymbol{\eta}_{ji}^{n} + \boldsymbol{\xi}_{ji}}{|\boldsymbol{\eta}_{ji}^{n} + \boldsymbol{\xi}_{ji}|}$$

$$s_{ji}^{n} = \frac{|\boldsymbol{\eta}_{ji}^{n} + \boldsymbol{\xi}_{ji}| - |\boldsymbol{\xi}_{ji}|}{|\boldsymbol{\xi}_{ji}|} \tag{33}$$

In the VBF-PD proposed in Section 3.2, the attenuation function $g(\boldsymbol{\xi}_{ji})$ should be incorporated into Eq. (33), such that $c = c_0 g(\boldsymbol{\xi}_{ji})$, with different forms summarised in Table 1. The central difference scheme is utilised to update velocity and acceleration (Silling and Askari 2005; Wriggers 2006):

$$\dot{\boldsymbol{u}}_{i}^{n+1/2} = \frac{\boldsymbol{u}_{i}^{n+1} - \boldsymbol{u}_{i}^{n}}{\Delta t}$$

$$\ddot{\boldsymbol{u}}_{i}^{n} = \frac{\boldsymbol{u}_{i}^{n+1} - 2\boldsymbol{u}_{i}^{n} + \boldsymbol{u}_{i}^{n-1}}{\Delta t^2} \tag{34}$$

where the notations $n+1$, n, $n-1$, $n+1/2$ represent numbers of time step ($n \geq 1$), termed as the updated step, current step, and the previous steps, respectively. Different time instants are denoted as follows:

$$t^{n+1} = t^{n} + \Delta t$$
$$t^{n+1/2} = (t^{n+1} + t^{n})/2 \tag{35}$$

Then, the displacement at time t^{n+1} can be calculated:

$$\boldsymbol{u}_{i}^{n+1} = \boldsymbol{u}_{i}^{n} + \dot{\boldsymbol{u}}_{i}^{n+1/2} \Delta t \tag{36}$$

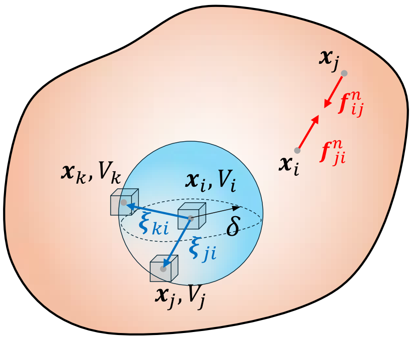

Fig. 4. Schematic of a 3D view of PD material points in the discretised domain.

5.2 Remarks on numerical discretization

The explicit time integration method is conditionally stable. Therefore, it is important to determine the maximum stable time increment $\Delta t_{\max}$. To achieve this, Silling and Askari (2005) proposed an efficient method for calculating $\Delta t_{\max}$, denoted as $\Delta t_{\max}^{\mathrm{S}}$. Alternatively, the Courant-Friedrichs-Lewy (CFL) method

(Mendes et al. 2019) is used to calculate the stable time increment, denoted as $\Delta t_{\max}^{\mathrm{CFL}}$. These two values can be computed as follows:

$$\Delta t_{\max}^{\mathrm{S}} = \sqrt{\frac{2\rho}{K_{\mathrm{eff}}}}, \quad \Delta t_{\max}^{\mathrm{CFL}} = \sqrt{\frac{h_{\mathrm{g}}^2 \rho}{K}} \tag{37}$$

where h_{g} represents the average space between PD points, K_{eff} is the effective stiffness (Silling and Askari 2005; Bobaru et al. 2016):

$$K_{\mathrm{eff}} = \sum_{j \in H_i} \frac{18K}{\pi \delta^4} \frac{V_j}{|\boldsymbol{\xi}_{ji}|} \tag{38}$$

In our program, the maximum stable time increment $\Delta t_{\max}$ is determined by:

$$\Delta t_{\max} = n_{\mathrm{safe}} \times \min\left(\Delta t_{\max}^{\mathrm{S}}, \Delta t_{\max}^{\mathrm{CFL}}\right) \tag{39}$$

where n_{safe} represents the safety factor ($0 < n_{\mathrm{safe}} < 1$).

Accurate calculation of the volume V_j for each PD point is essential for correctly capturing mechanical responses. The conventional calculation method assumes a regular shape, specifically a sphere with radius δ. However, as shown in Fig. 4, V_j is not always entirely covered by a sphere. For example, at the edge of the sphere, V_j may be partially covered within δ, which requires a correction in volume calculation (Parks et al. 2008; Bobaru and Zhang 2015). The correction factor associated with $\boldsymbol{x}_j$ is written as:

$$\alpha_j^{\mathrm{c}} = \frac{2\delta + h_{\mathrm{g}}}{2h_{\mathrm{g}}} - \frac{R_{ji}}{h_{\mathrm{g}}} \tag{40}$$

Then, the corrected volume $V_j{}'$ is written as:

$$V_j{}' = \begin{cases} \alpha_j^{\mathrm{c}} V_j, & \text{if } \left(\delta - \bar{h}\right) \le R_{ji} \le \delta \\ V_j, & \text{if } R_{ji} \le \bar{h} \\ 0, & \text{if } \delta > R_{ji} \end{cases} \tag{41}$$

where R_{ji} is the effective radius, expressed by $|\boldsymbol{\xi}_{ji} + \boldsymbol{\eta}_{ji}^{n}|$, and $\bar{h} = h_{\mathrm{g}}/2$.

6. Results and discussion

In this section, the VBF-PD is validated through benchmark tests. Then, the damage characteristics of particles are examined, taking into account the effects of material properties, particle arrangements, and loading conditions.

6.1 Validation of the proposed VBF-PD model

Three representative benchmark tests are selected to validate the VBF-PD, including: (1) the Kalthoff-

Winkler test, (2) cylinder impact test, and (3) single particle crushing test, wherein the numerical performances, especially the grid convergence property and numerical accuracy, are studied in detailed.

6.1.1 The Kalthoff-Winkler test

The Kalthoff-Winkler (KW) test is a classical benchmark test widely used for validating numerical methods in simulating dynamic damage (Madenci and Oterkus 2013; Diehl et al. 2019). As shown in Fig. 5, a 3D KW model is constructed and discretised into peridynamic points. The impactor is assumed to be a rigid body and impacts the brittle material at a velocity v_0 along the *z*-axis. In the brittle material, two pre-existing cracks of length l_c and width a_0, are placed in the vertical direction, separated by a distance d_c. The parameters used in the simulation are provided in Table 2. The data is obtained from literature (Ren et al. 2019; Zhang et al. 2022). Analogous to previous studies, for convenience, we compare the initiation angle of the pre-existing cracks with the experimental result. Figs. 5c-5e illustrate the damage patterns and crack paths during the impact process. The initiation angle is consistent with the reference result. The dynamic cracks propagate at an angle of approximately 30° to the horizonal direction. The two cracks propagate in a symmetric pattern. In addition, it demonstrates that the proposed VBF-PD is capable of effectively capturing the growth of dynamic cracks. More quantitative analyses regarding numerical performances will be presented in Sections 6.1.2 and 6.1.3.

Table 2

Model parameters used in peridynamic simulations.

Model parameter	**Kalthoff-Winkler test**	**Cylinder impact test**	**Single particle test**	**Particle system test**	**Unit**
Young's modulus E	190	100	100	100, 150, 200, 250, 300	GPa
Poisson's ratio ν	0.25	0.25	0.25	0.25	-
Shear modulus G	76	40	40	40, 60, 80, 100, 120	GPa
Material density ρ	8000	2800	2650	2650	kg/m^3
Critical energy release rate G_c	2.2×10^4	1×10^{10} (no failure)	10	10, 20, 30, 50	J/m^2
Impact velocity v_0	32	20	0.1 ~ 10	5, 10, 20, 30	m/s
Dimensions	$L = 0.2$, $W = 0.03$ $H = 0.1$ $l_c = 0.05$, $a_0 = 0.001$ $d_c = 0.05$	$H = 0.4$, $R_1 = 0.4$ $R_2 = 0.1$	$R_1 = 1$, $R_2 = 1$	$R_1 = 2$, $R_2 = 1$	m m
Horizon δ	$3h_g$	$3h_g$, $5h_g$	$3h_g$	$3h_g$	m
Grid resolution h_g	0.02	0.04, 0.02, 0.015, 0.008	0.008	0.008	
Time increment Δt	3.6×10^{-8}	2.1×10^{-8}	2.2×10^{-8}	2.2×10^{-8}	s

Remarks: Data source of the Kalthoff-Winkler test: Ren et al. (2019) and Zhang et al. (2022). Data source of particle crushing tests: Zhu and Zhao (2019) and Wan et al. (2020).

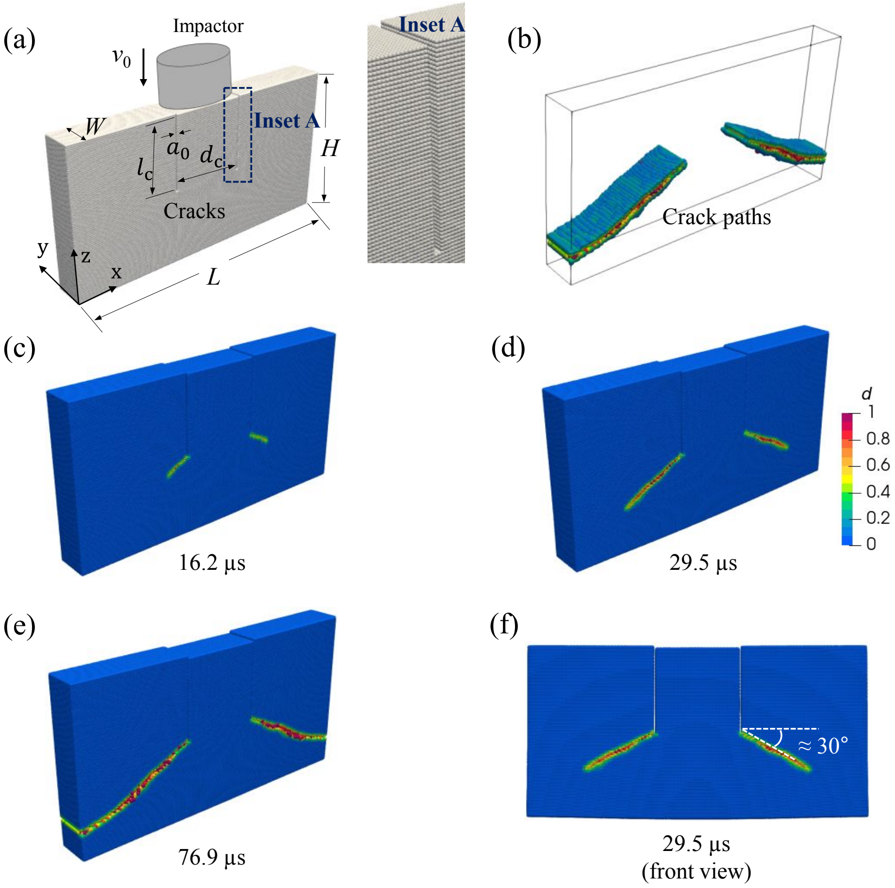

Fig. 5. The Kalthoff-Winkler test: (a) Schematic of the model and peridynamic points; (b) A 3D view of crack paths; (c)-(e) Damage pattern at various time instants; (f) A font view of crack paths.

6.1.2 Contact impact on a cylinder: different VBF forms

As illustrated in Fig. 6a, a cylinder impact model is constructed to examine the numerical accuracy and convergence property of the proposed VBF-PD. The radii of the deformable cylinder and the rigid impactor are denoted as R_1 and R_2, respectively, and the height of the cylinder is H. Notably, in the convergence analysis, the grid resolution, defined as the spacing between PD points, is set to 0.04, 0.02, 0.015, and 0.008. The material is purely deformable, and no failure occurs, such that the critical energy density rate G_c is set to a very high value. Detailed parameters are provided in Table 2.

The VBF-PD formulation described in Section 3.2 introduces a key improvement by replacing the conventional micromodulus function with the variable bond force density functions, as shown in Table 1 and Fig. 2a. To evaluate its performance, we compare the total kinetic energy (E_k) values calculated using different VBF forms. The results obtained from a commercial FEM software ABAQUS (Smith 2009) are used as the reference solution. E_k of mechanical system is computed though the summation of discrete kinetic energy e_k over all material points (in PD) or elements (in FEM), written as:

$$E_k = \sum_{i=1}^{n_p} e_{k,i} = \sum_{i=1}^{n_p} \frac{1}{2} \rho V_i \left(v_1^2 + v_2^2 + v_3^2\right) \tag{42}$$

where n_p represents the number of material points or elements involved in this computation, and v_j $(j =$

1,2,3) are the velocity components of material point i.

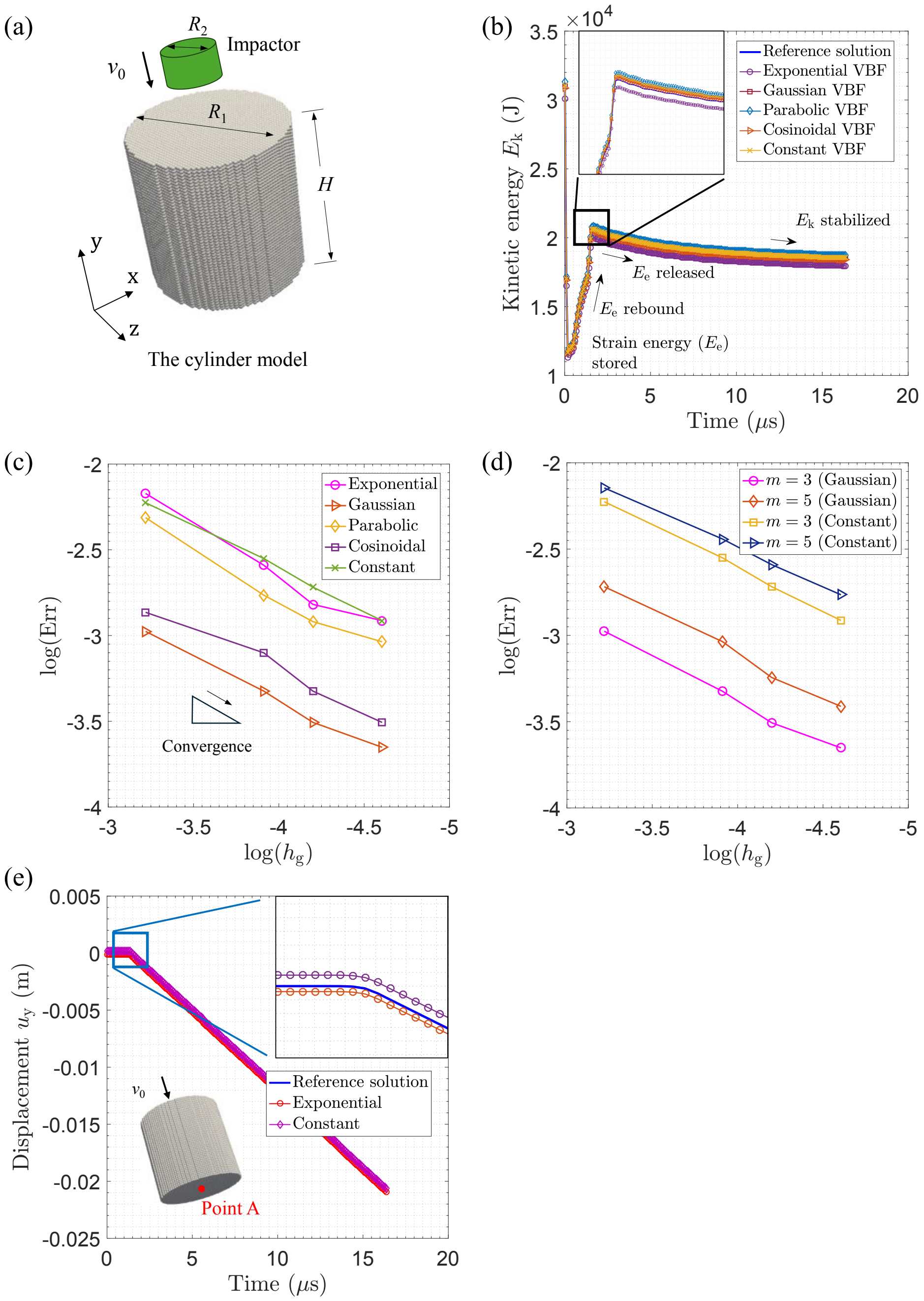

Fig. 6. The cylinder impact test: (a) Schematic of the model and peridynamic points; (b) Variation of kinetic energy E_k; (c) Convergence of the VBF-PD with various VBF forms; (d) Convergence of the VBF-PD with various peridynamic horizons ($\delta = m\ h_\mathrm{g}$); (e) Variation of vertical displacement.

The variation of E_k, computed using different VBFs, are depicted in Fig. 6b. It is observed that, at the initial time, the kinetic energy is on the order of 3×10^4 J. Then, after a short period, E_k decreases to the order of 1×10^4, with the reduced portion transferred into the strain energy E_e. Eventually, the kinetic energy E_k tends to stabilize. In the inset of Fig. 6b, the result calculated by the Parabolic VBF is relatively smaller than those from other methods, while the Gaussian VBF is relatively accurate compared with others. However, despite the errors, they are acceptable and do not significantly affect the overall performance.

A further analysis of grid convergence performance evaluation is conducted under varying grid resolutions h_{g} and different VBF forms. As displayed in Figs. 6c and 6d, the x- and y-axes are scaled logarithmically to clearly show the variation trends. The relative error, denoted as Err, is defined as:

$$\mathrm{Err} = \sum_{i=1}^{n_{\mathrm{p}}} \frac{\|\tilde{x}_i - x_i^{\mathrm{h}}\|_2}{\|\tilde{x}_i\|_2} \tag{43}$$

where $\tilde{x}_i$ and x_i^{h} represent the reference solutions and the solutions obtained by the proposed method, respectively. The simulation results demonstrate that the error associated with the conventional VBF is relatively larger compared to other methods, whereas the Gaussian VBF exhibits higher accuracy. The convergence rates of all methods are similar as the grid resolution increases. As shown in Fig. 6d, the error computed with m = 3 is lower than that computed with m = 5. This observation is consistent with many existing studies (Chen et al. 2023; Wang and Yin 2024b).

Fig. 6e shows the variation of the displacement component u_y at the bottom of the cylinder calculated using different VBF forms. u_y remains approximately zero until 1.5 μs. This delay is caused by the dynamic disturbance not yet propagating to the bottom point. The phenomenon is referred to as the dynamic effect of elastic waves, which is absent under static conditions. Then, the magnitude of displacement $|u_y|$ increases monotonically util the simulation termination. As an illustration, Fig. 7 presents the contours of deformation patterns during impact, where the wavefront of the elastic waves can be clearly observed. From 0.2 μs to 1.2 μs, the wavefront propagates an obvious distance in such short period.

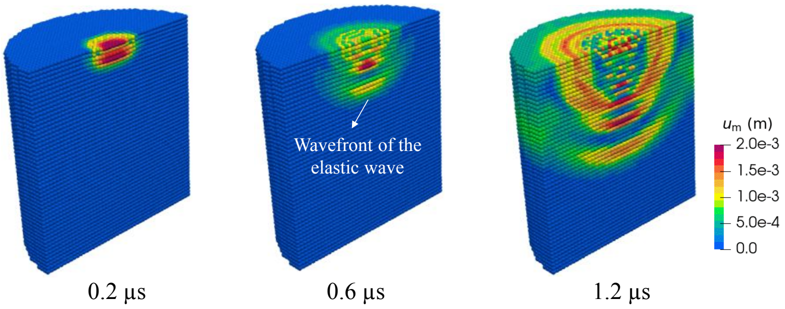

Fig. 7. Deformation patterns (elastic wave propagation) of the cylinder. The slice view shows a half of the model.

6.1.3 Single particle crushing: comparison of crushing patterns

The single particle crushing test has been widely used in previous studies for computational particle mechanics (Zhao et al. 2015; Zhu and Zhao 2019; Wan et al. 2020; Blanc et al. 2021; Walayat et al. 2023). A single particle model discretized by PD material points is depicted in Fig. 8a. An impactor with radius R_2 moves at velocity v_0 and strikes the particle, acting either as a rigid indenter or as a rigid particle. Model parameters are given in Table 2.

The cracks propagates during the impact process. As a comparative analysis, we compare the results calculated by the VBF-PD with the existing simulation results (Zhu and Zhao 2019; Wan et al. 2020), and experimental results (Zhao et al. 2015). Fig. 8 demonstrates that the damage pattern simulated using our proposed method agrees well with those in existing literature. It appears that four main cracks are generated around the impact position and gradually propagate to the bottom edge of the particle. Note that the model parameters are consistent with those used in their studies. A quantitative analysis associated with the contact force-velocity curves is presented in Fig. 9. The reference solutions are extracted from the results by Zhu and Zhao (2019). This demonstrates that the proposed method can appropriately reproduce the existing results.

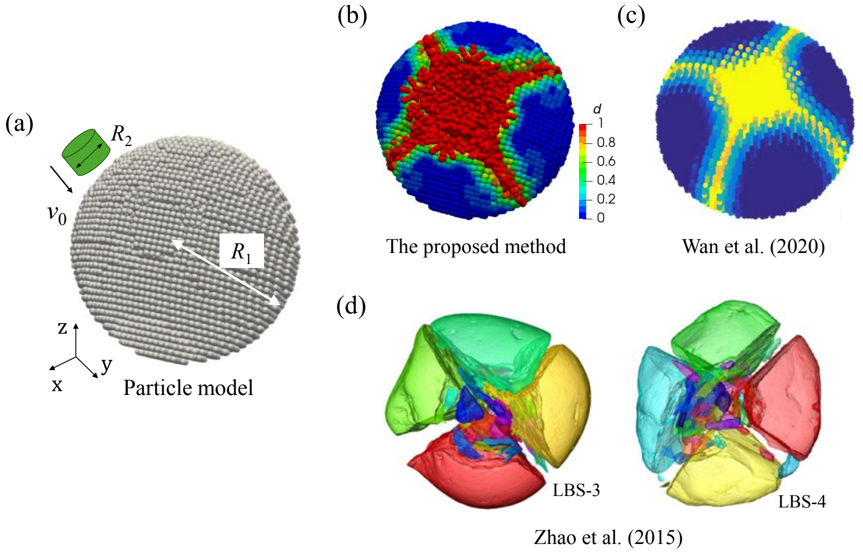

Fig. 8. The single particle crushing test: (a) Schematic of the model and peridynamic points; (b) Results simulated by the VBF-PD; (c)-(d) The existing results (Zhao et al. 2015; Wan et al. 2020) of the Leighton Buzzard sand (LBS-3 and LBS-4).

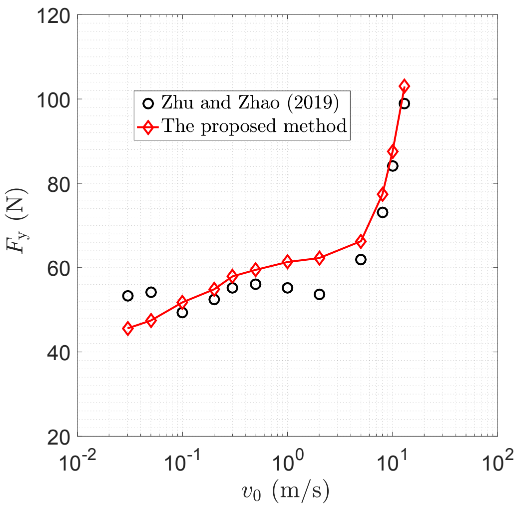

Fig. 9. Comparison with existing results for the variation in contact force F_y with increasing impact velocity v_0 (Zhu and Zhao 2019).

6.2 *Crushing of particle pair with different material properties*

Consider a particle pair system, where a rigid impactor strikes the particle pair at an initial velocity, following the same settings as described in Section 6.1.3. The test investigates the effects of Young's modulus E, impact velocity v_0 and critical energy release rate G_c on failure patterns. Unless stated otherwise, the model parameters are listed in Table 2.

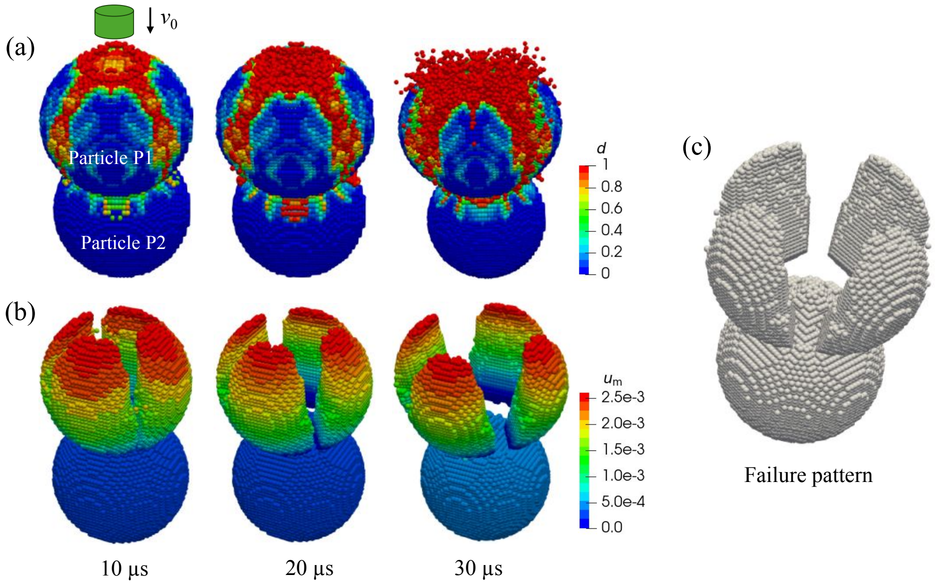

Fig. 10. Damage and displacement of double particle: (a) Damage evolution; (b) Displacement distribution (only the undamaged portions are visualised); (c) A failure pattern at 30 μs.

Figs. 10a and 10b display the damage patterns and displacement distributions of the particle pair over a time sequence. The target particle is denoted as Particle P1, while the bottom particle is denoted as Particle P2. Damage zones propagate from P1 to P2, with the most severe damaged regions concentrated at the interface of P1-P2. Particle P1 fragments into four main segments, as shown in Fig. 10b. For clarity, only the undamaged portions are displayed. These four portions do not undergo significant further breakage; instead, the openings between them vary, forming a flower-like pattern, as illustrated in Fig. 10c.

Then, the dynamic damage characteristics are examined under varying impact velocity v_0 and Young's modulus E. By comparing the results in Figs. 11a and 11b, we observe that v_0 significantly influences the damage pattern. A higher impact velocity has considerable influence on damage development, as the top particle is almost entirely fragmented at v_0 = 30 m/s, whereas it is only partially fragmented at v_0 = 10 m/s. A comparison between Figs. 11a and 11c reveals the effect of Young's modulus E on particle breakage. With a fixed velocity of v_0 = 10 m/s, the crack paths and damage pattern of the bottom particle under E = 200 GPa are more severe than those under E = 100 GPa. An underlying reason is that an increase in E enhances the stiffness of particles, thereby promoting a more efficient transfer of kinetic energy from the top particle to the bottom one. Increase in Young's modulus E alters the distribution of crack paths, reducing the number of dispersed fissures as material stiffness strengthened. The results also indicate that the increase in E does not guarantee prevention of cracks; in fact, conversely, cracks may propagate further in stiffer materials compared to weaker materials.

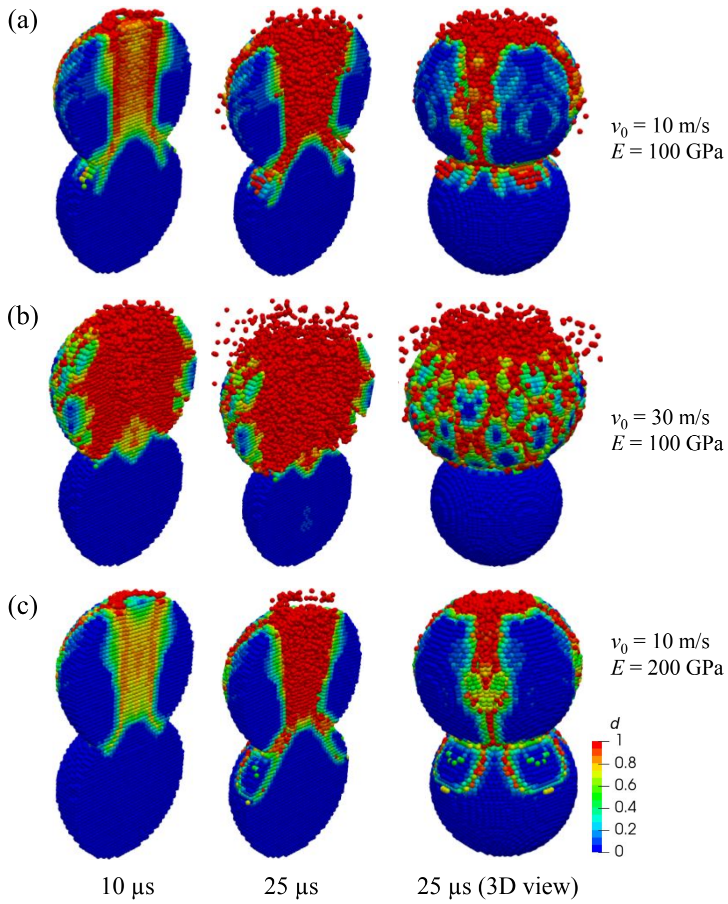

Fig. 11. Failure patterns of double particles with different impact velocities v_0 and elastic moduli E. The slice views illustrate a half of the 3D model: (a) v_0 = 10 m/s, E = 100 GPa; (b) v_0 = 30 m/s, E = 100 GPa; (c) v_0 = 10 m/s, E = 200 GPa.

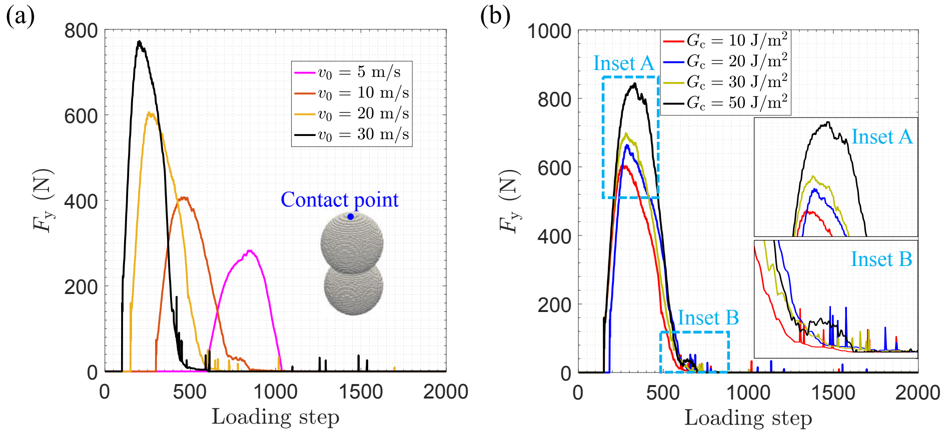

Fig. 12. Variation of contact force at the impact position: (a) Contact force under various impact velocities; (b) Contact force under various energy release rates.

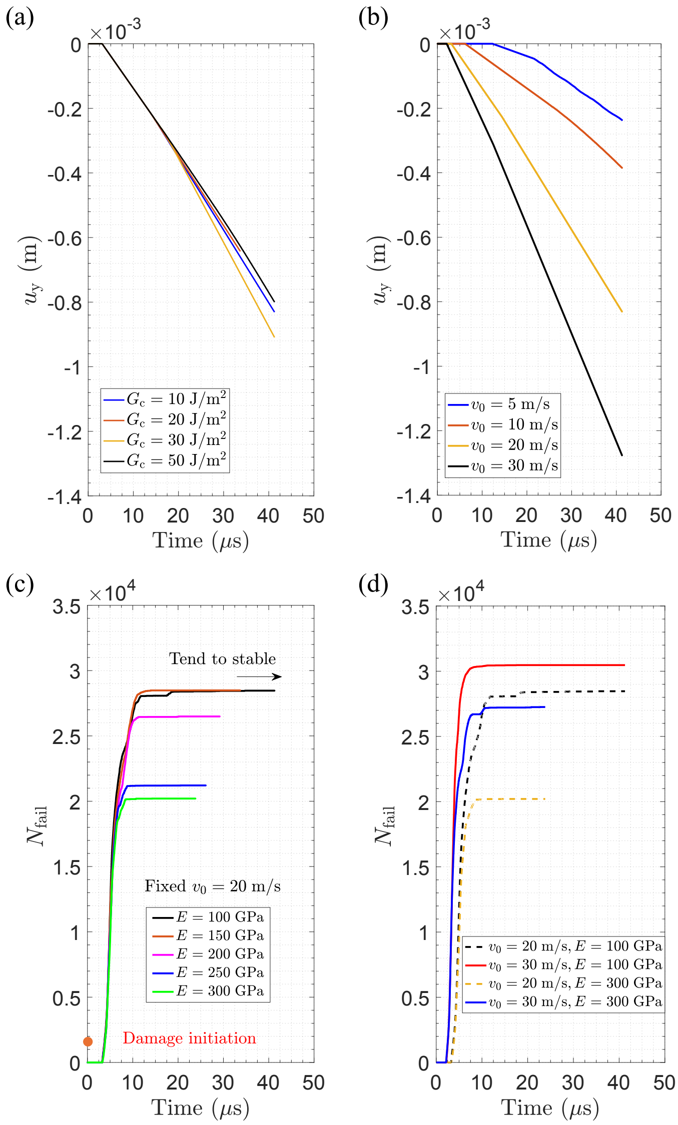

Fig. 13. Variations of contact force and broken PD bonds: (a)-(b) Comparison of the effects of energy release rate and impact velocity on displacement at the contact point; (c)-(d) Effects of Young's modulus and impact velocity on damage.

The contact force at the impact position, denoted as F_y, is calculated using the VBF-PD. Fig. 12a shows that variation in impact velocity v_0 alters the position at which the maximum F_y occurs. A lower v_0 leads to a later occurrence of the maximum F_y. In addition, slight fluctuations are observed after loading step 1000, which can be attributed to the ongoing interactions among PD points. At lower values of v_0 (5 or 10 m/s), these fluctuations disappear. In contrast to the effect of v_0, Fig. 12b illustrates the effect of the critical energy release rate G_c on the contact force F_y, where the maximum F_y consistently appears around loading step 250.

Figs. 13a and 13b demonstrates that the variation in the impact velocity v_0 has a greater effect on deformation than the variation in G_c. The y-axis, u_y, represents the vertical displacement at the contact position. It is worth noting that the horizontal displacement u_x vanishes because the impact is applied along the vertical direction. In the simulation, we record the variation in the number of broken PD bonds during dynamic damage, denoted as N_{fail}, as defined in Eq. (22). As displayed in Figs. 13c and 13d, N_{fail} captures damage characteristics and gradually tends to stabilise. Fig. 13c shows that an increase in Young's modulus E highly reduces N_{fail}, as a higher E enhances particle stiffness. For comparison, Fig. 13d illustrates the combined effect of v_0 and E on damage. The results are consistent with physical expectations, showing that N_{fail} reaches its maximum under a higher v_0 and a lower E. For example, N_{fail} at v_0 = 30 m/s and E = 100 GPa is greater than at v_0 = 20 m/s and E = 300 GPa.

6.3 Different arrangements: effect of connection angle

The preceding analysis focuses on the central collision of a particle pair. However, in real scenarios, the connection angle, denoted as α, may alter particle morphology and microstructure. In this context, impact often occur off-centre, with particle pairs arranged at a connection angle α, as illustrated in Fig. 14. We examine the influence of different connection angles on particle crushing, with α = 20°, 45°, 70°, and 90°. Model parameters are provided in Table 2.

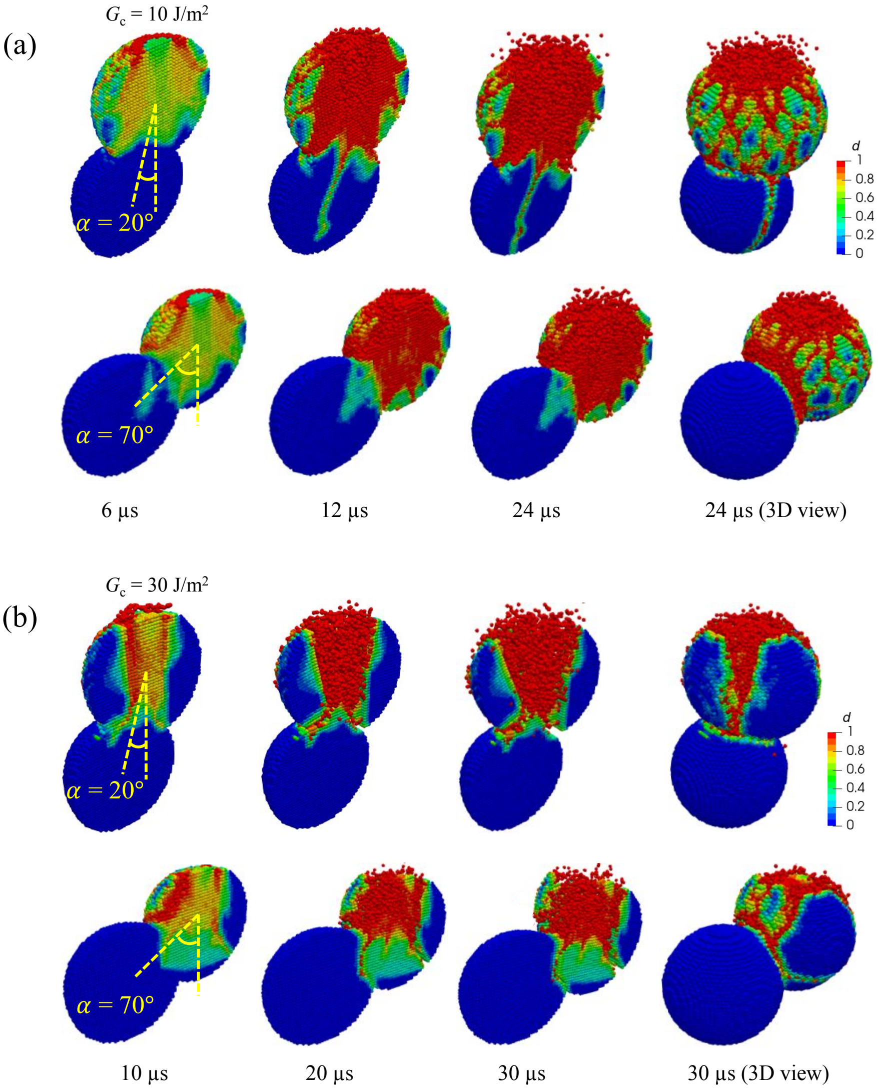

Fig. 14. Damage evolution of double pairs with different arrangements (α = 20° and 70°). The slice views and their corresponding 3D views using different critical energy release rates: (a) G_c = 10 J/m²; (b) G_c = 30 J/m².

Fig. 14 illustrates the damage patterns at different stages when $\alpha = 20°$ and 70°, and the critical energy release rates $G_\mathrm{c} = 10$ and 30 J/m^2. The results indicate that increasing the material strength (by raising G_c) delays the onset of damage. For example, the damaged regions observed at 6 μs for $G_\mathrm{c} = 10$ J/m^2 (Fig. 14a) are significantly more extensive than those at 10 μs for $G_\mathrm{c} = 30$ J/m^2 (Fig. 14b). A large crack even propagates vertically in the former case, while it is absent in the latter case. The severely damaged regions are mainly concentrated in a central band of the top particle if $G_\mathrm{c} = 30$ J/m^2. In contrast, when $G_\mathrm{c} = 10$ J/m^2, the entire top particle is almost completely fragmented. In both cases, the interface between the top and bottom particles is fragmented due to high strain gradients and stress concentration. The top particle directly interacts with the impactor and absorbs most of the impact energy. In contrast, crushing of the bottom particle is mitigated by the buffering effect, which becomes more pronounced with increasing G_c.

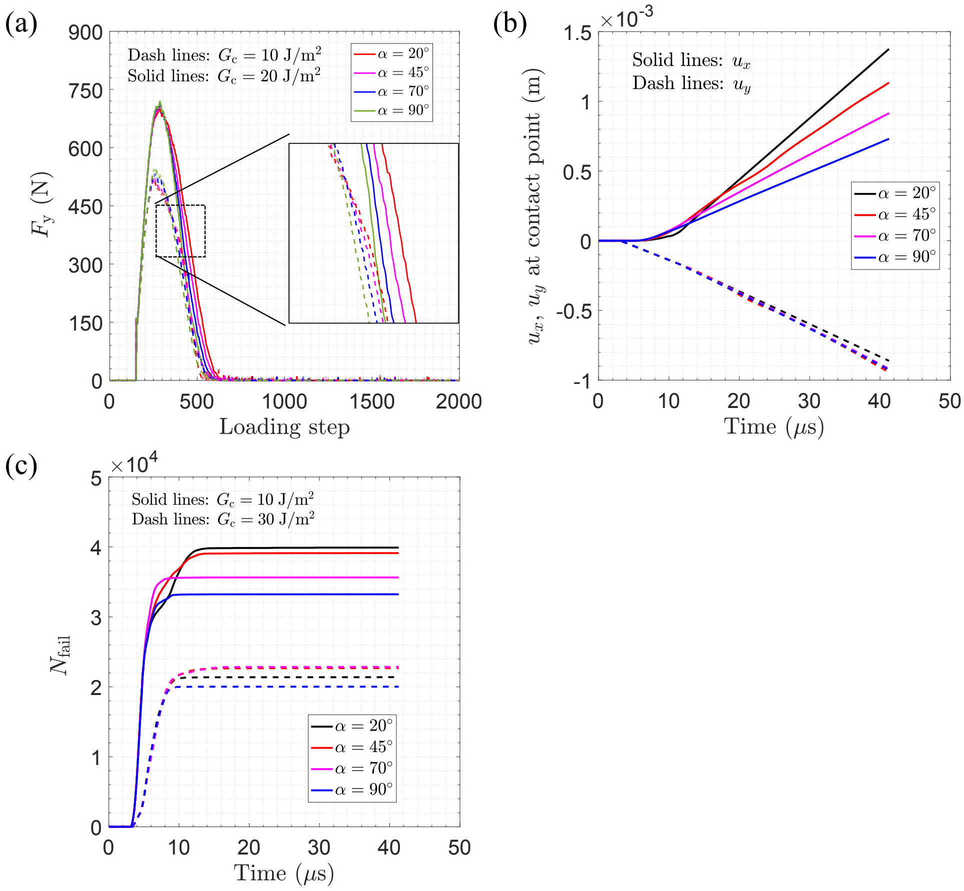

Fig. 15. Variations of contact force and broken PD bonds under different particle arrangements: (a) Variation of contact force; (b) Variation of displacements at the contact position; (c) Variation of number of broken PD bonds.

The force-loading step curves are recorded and compared under various conditions. As shown in Fig. 15a, the change of connection angle α does not significantly alter variation of these curves. The peak values of F_y under conditions of $G_\mathrm{c} = 10$ J/m^2 and 30 J/m^2 are approximately 530 and 750 N, respectively. An Increase in α slightly shifts the curve along the positive direction of the *x*-axis, caused by the off-centre effect in the impact process. To further illustrate the off-centre effect, which occurs when $\alpha \neq 0°$, we record the variation of displacement components u_x and u_y at the contact position, as displayed in Fig. 15b. It is worth noting that the horizontal displacement u_x vanishes when $\alpha = 0°$. While the change of α does not significantly affect u_y, it strongly influences u_x. This is because different arrangements of particles alter the positions of the barycentre, causing the motion and deformation of the particle system to vary in each case.

Fig. 15c depict the effects of critical energy release rate G_c and connection angle α on the number of broken PD bonds N_fail. It is evident that a considerable amount of bonds break during particle crushing. The effect of G_c on damage is much greater than that of α. Within the range of α = 20° ~ 90°, decease in α may increase N_fail, because the smaller the angle, the lesser the off-centre effect, allowing the impact energy to be fully transferred into the bottom particle. In contrast, when α approximates 90°, this effect is not as pronounced. A common feature is that the variation of N_fail tends to stabilise over time.

6.4 A complex scenario: crushing of aggerated particles

Many studies have highlighted that geometric parameters of particle systems strongly influence damage characteristics (de Gennes 1998; Zhao et al. 2015, 2023; Buscarnera and Einav 2021). In this section, we study crushing properties of a particle aggregation. As shown in Fig. 16a, the model consists of six particles, denoted as P1, P2, …, P6. The average connection angle between P1 and its neighbouring particles (P2, P3, P4, and P5) is denoted as $\bar{\alpha}$. The distance between particles is denoted as $\overline{r_\mathrm{p}}$. We investigate variations in the parameters $\bar{\alpha}$ (20° and 45°) and $\overline{r_\mathrm{p}}$ (2.8 and 3.6 mm). Other parameters are the same as those used in Section 6.3. For illustration, Figs. 16b-16d display three different patterns of particle arrangements.

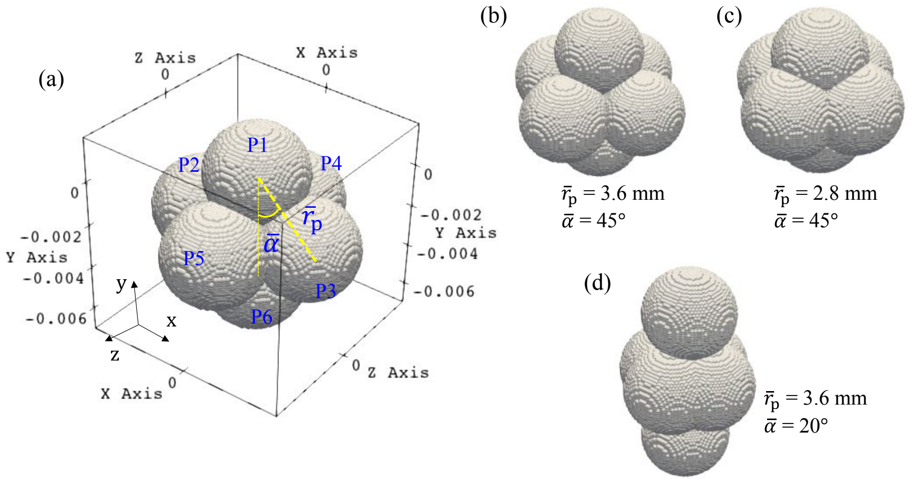

$\bar{r}_\mathrm{p}$ = 3.6 mm
$\bar{\alpha}$ = 45°

$\bar{r}_\mathrm{p}$ = 2.8 mm
$\bar{\alpha}$ = 45°

$\bar{r}_\mathrm{p}$ = 3.6 mm
$\bar{\alpha}$ = 20°

Fig. 16. Different patterns of a particle aggregation: (a) Schematic of the model and peridynamic model; (b) $\overline{r_\mathrm{p}}$ = 3.6 mm, $\bar{\alpha}$ = 45°; (c) $\overline{r_\mathrm{p}}$ = 2.8 mm, $\bar{\alpha}$ = 45°; (d) $\overline{r_\mathrm{p}}$ = 3.6 mm, $\bar{\alpha}$ = 20°. The parameters $\bar{r}_\mathrm{p}$ and $\bar{\alpha}$ represent the average distance and the average connection angle between particle pairs P1-Pk ($k = 2,3,4,5$), respectively.

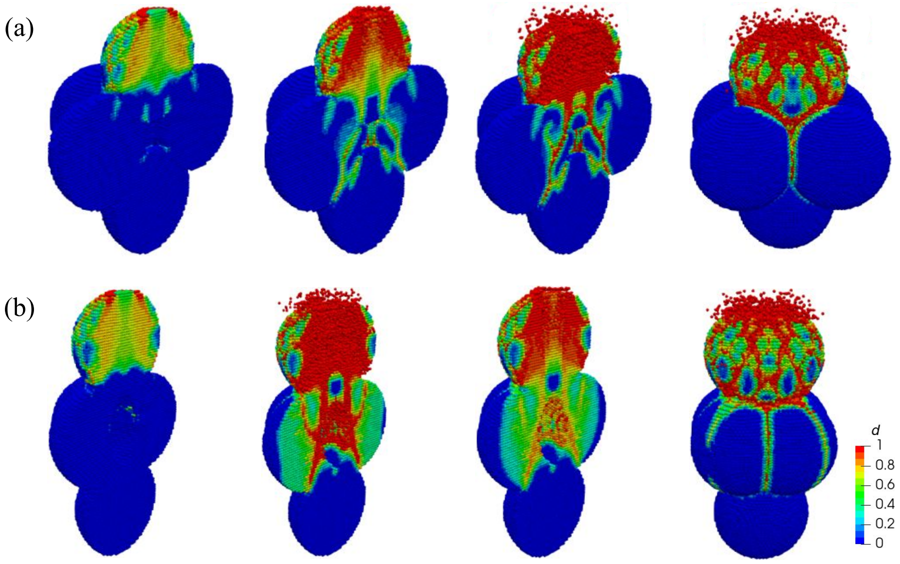

Fig. 17. Damage evolution of a particle aggregation: (a) $\overline{r_{\mathrm{p}}}$ = 3.6 mm, $\bar{\alpha}$ = 45°; (b) $\overline{r_{\mathrm{p}}}$ = 3.6 mm, $\bar{\alpha}$ = 20°. The critical energy release rate G_{c} = 30 J/m^2.

In Fig. 17, $\overline{r_{\mathrm{p}}}$ = 3.6 mm is fixed, while $\bar{\alpha}$ is varied to examine the effect of the connection angle on crushing. When $\bar{\alpha}$ = 20°, cracks propagate into particles P2, P3, P4, and P5, even cause partial damage to particle P6. In contrast, when $\bar{\alpha}$ = 45°, the damage regions are primarily concentrated at the interfaces between particles. To further analyse the influences of $\bar{\alpha}$, $\overline{r_{\mathrm{p}}}$ and G_{c} on the contact force F_y, we calculate the difference ΔF_y between the solutions of two cases among conditions C0, C1, C2, and C3, expressed as $\Delta F_y = F_y^{C0} - F_y^{Ci}$ $(i = 1{,}2{,}3)$, as illustrated in Fig. 18a. The peak values of ΔF_y primarily occur within the loading step range of 400 ~ 700. After loading step 1000, there are still some fluctuations in ΔF_y until the simulation terminates. Fig. 18b shows that changes in $\bar{\alpha}$, $\overline{r_{\mathrm{p}}}$ and G_{c} do not considerably affect the occurrence position of the peak F_y, which is also mainly observed within the loading step range of 400 ~ 700. This indicates that these factors mainly influence the peak values. Moreover, increases in both $\bar{\alpha}$ and G_{c} enhance the peak value of F_y, while $\overline{r_{\mathrm{p}}}$ has the opposite effect.

The variation of the global damage factor D_{g} (Eq. (22)) is shown in Fig. 18c. An increase in G_{c} not only supresses the growth of D_{g} but also alters the shape of its evolution curves. Specifically, when G_{c} = 10 J/m^2 and r_{p} = 3.6 mm, the damage factor D_{g} calculated with $\bar{\alpha}$ = 45° is lower than that calculated with $\bar{\alpha}$ = 20°. Conversely, under the conditions of G_{c} = 30 J/m^2 and r_{p} = 3.6 mm, the trend is reversed. By comparing the blue and black solid lines in Fig. 18c, it is evident that when only $\bar{\alpha}$ is varied under G_{c} = 30 J/m^2, the value of D_{g} will eventually converge to nearly the same constant. Therefore, a phenomenon observed under lower G_{c} condition (10 J/m^2) may not be evident under higher G_{c} condition (30 J/m^2), owing to the complex interactions among multiple particles.

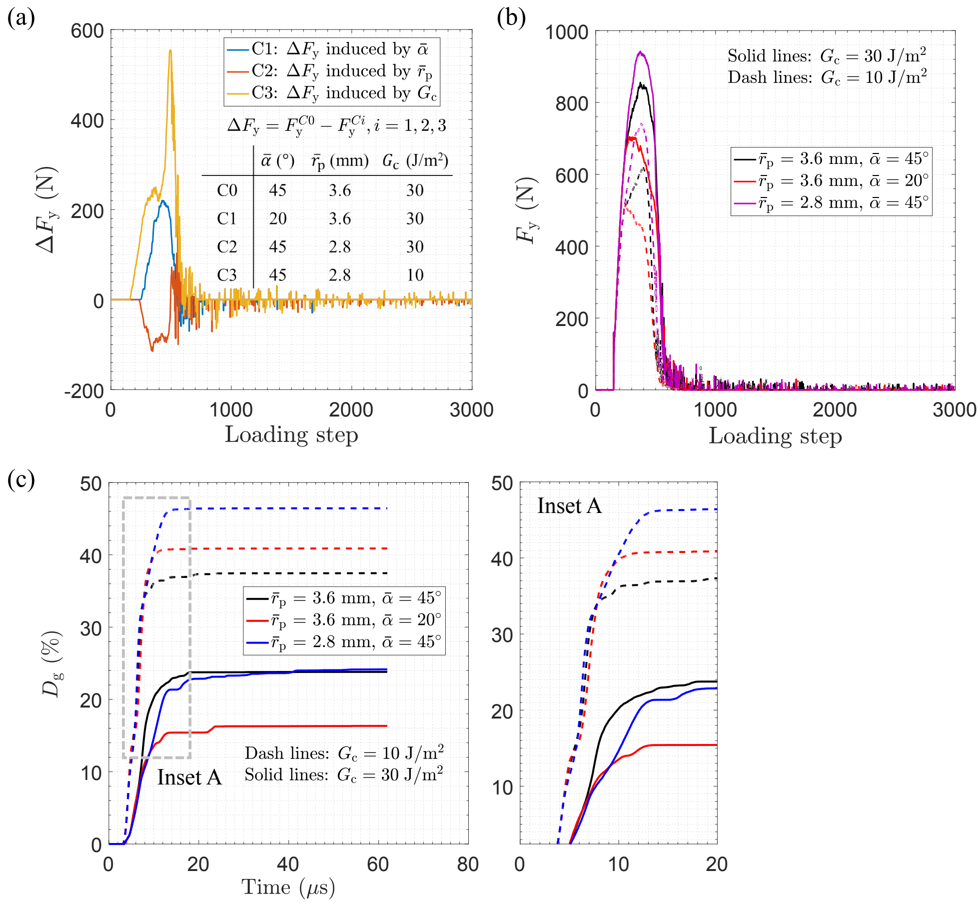

Fig. 18. Variations of contact force and damage factor: (a) Variation of contact force F_y; (b) Variation of contact force increment ΔF_y; (c) Variation of global damage D_g over time under different conditions.

7. Concluding remarks

In this work, we proposed an improved variable bond force (VBF) peridynamic model for simulating dynamic damage of 3D particles. The VBF-PD framework integrates multiple forms of VBF, enabling the bond force density to vary with distance in a physically consistent manner. An improved dynamic damage model was developed to capture breakage. Furthermore, efficient constraint strategies are developed to handle particle-particle and impactor-particle interactions. The proposed method extends the applicability of conventional PD to complex dynamic fragmentation problems. Based on the VBF-PD, numerical performance was examined through benchmark tests. Different VBF forms were applied to examine gird convergence. Several particle crushing tests were conducted under various particle arrangements, loadings, and material properties. The evolution of kinetic energy, contact force, and damage factor was thoroughly analysed. The results show that particle crushing can be mitigated by the buffering effect through increasing the critical energy release rate. Different particle arrangements may lead to variations in particle motion and deformation. Damage evolution mode of multiple-particle systems differs from those observed in few-particle systems, which can be attributed to the complex interactions among multiple particles.

The VBF-PD can be further extended to simulate large systems consisting of thousands of particles. A cost-effective approach is required to detect simultaneous particle contacts (Konrad and Salami 2018; Neto 2023). Moreover, the VBF-PD can be extended to account for the breakage of irregularly shaped particles

(Azéma et al. 2013; Huang et al. 2015b, 2023), thereby offering insights into the influence of particle morphology on particle breakage.

Conflicts of Interest

The authors declare no conflicts of interest.

Data Availability Statement

Data generated or analyzed during this study are available from the corresponding author upon reasonable request.

Acknowledgments

This research was financially supported by the Open Research Fund of State Key Laboratory of Geomechanics and Geotechnical Engineering Safety, Institute of Rock and Soil Mechanics, Chinese Academy of Sciences (Grant number: SKLGGES-024014) and the Research Grants Council of the Hong Kong Special Administrative Region (Grant numbers: T22-607/24-N, 15227923, 15229223).

CRediT authorship contribution statement

Luyu Wang: Methodology, Formal analysis, Software, Validation, Visualisation, Writing - original draft. **Zhen-Yu Yin:** Funding acquisition, Supervision, Formal analysis, Writing - review & editing. **Weizhong Chen:** Supervision, Formal analysis, Writing - review & editing.

Appendices

Appendix A. The initial micromodulus in VBF-PD for 3D problem

Following Section 3.2, various forms of the attenuation function $g(\xi)$ are used to derive the expressions for the initial micromodulus c_0. We consider five different forms of the variable bond force (VBF): (1) Exponential function; (2) Gaussian function; (3) Parabolic function; (4) Cosinoidal function; (5) Constant. The expressions are given as:

$$g(\boldsymbol{\xi}) = \begin{cases} \mathrm{e}^{-\frac{|\boldsymbol{\xi}|}{\delta}}, & \text{Exponential VBF} \\ \mathrm{e}^{-\left(\frac{\xi}{\delta}\right)^2}, & \text{Gaussian VBF} \\ \left(1-\left(\frac{\xi}{\delta}\right)^2\right)^2, & \text{Parabolic VBF} \\ \cos\frac{\pi\boldsymbol{\xi}}{2\delta}, & \text{Cosinoidal VBF} \\ 1, & \text{Constant VBF} \end{cases} \tag{A.1}$$

where the meanings of all notations have been introduced in the proceeding sections.

To derive the expression of c_0 in the VBF-PD, under dilatant condition, the strain energy density W^{CM} in continuum mechanics can be obtained by substituting the loading condition $\varepsilon_{kk} = s_0,\ (k = 1,2,3)$ into Eq. (19), resulting in:

$$W^{\mathrm{CM}} = \frac{1}{2}\lambda(\varepsilon_{kk}\varepsilon_{kk})^2 + \mu\varepsilon_{ij}\varepsilon_{ij} = \frac{3}{2}\frac{E}{(1-2\nu)}s_0^2 \quad \text{(dilatant condition)} \tag{A.2}$$

The strain energy density W^{PD} (Eq. (18)) in PD can be expressed in different forms by substituting different forms of $g(\boldsymbol{\xi})$ (Eq. (A.1)), given as:

Exponential VBF:

$$W^{\mathrm{PD}} = \frac{1}{2}\int_0^{\delta}\int_0^{2\pi}\int_0^{\pi} \mathrm{e}^{-\frac{|\boldsymbol{\xi}|}{\delta}}\left(c_0\frac{s_0^2|\boldsymbol{\xi}|^3}{2}\sin\varphi\right)\mathrm{d}\varphi\,\mathrm{d}\theta\,\mathrm{d}|\boldsymbol{\xi}| = \pi c_0\delta^4 s_0^2\left(6-\frac{16}{\mathrm{e}}\right) \tag{A.3}$$

Gaussian VBF:

$$W^{\mathrm{PD}} = \frac{1}{2}\int_0^{\delta}\int_0^{2\pi}\int_0^{\pi} \mathrm{e}^{-\left(\frac{\xi}{\delta}\right)^2}\left(c_0\frac{s_0^2|\boldsymbol{\xi}|^3}{2}\sin\varphi\right)\mathrm{d}\varphi\,\mathrm{d}\theta\,\mathrm{d}|\boldsymbol{\xi}| = \pi c_0\delta^4 s_0^2\left(\frac{1}{2}-\frac{1}{\mathrm{e}}\right) \tag{A.4}$$

Parabolic VBF:

$$W^{\mathrm{PD}} = \frac{1}{2}\int_0^{\delta}\int_0^{2\pi}\int_0^{\pi}\left(1-\left(\frac{\xi}{\delta}\right)^2\right)^2\left(c_0\frac{s_0^2|\boldsymbol{\xi}|^3}{2}\sin\varphi\right)\mathrm{d}\varphi\,\mathrm{d}\theta\,\mathrm{d}|\boldsymbol{\xi}| = \frac{\pi c_0\delta^4 s_0^2}{24} \tag{A.5}$$

Cosinoidal VBF:

$$W^{\mathrm{PD}} = \frac{1}{2}\int_0^{\delta}\int_0^{2\pi}\int_0^{\pi}\cos\frac{\pi\boldsymbol{\xi}}{2\delta}\left(c_0\frac{s_0^2|\boldsymbol{\xi}|^3}{2}\sin\varphi\right)\mathrm{d}\varphi\,\mathrm{d}\theta\,\mathrm{d}|\boldsymbol{\xi}| = \frac{2}{\pi^3}c_0\delta^4 s_0^2(\pi^3-24\pi+48) \tag{A.6}$$

Constant VBF:

$$W^{\mathrm{PD}} = \frac{1}{2}\int_0^{\delta}\int_0^{2\pi}\int_0^{\pi}\left(c_0\frac{s_0^2|\boldsymbol{\xi}|^3}{2}\sin\varphi\right)\mathrm{d}\varphi\,\mathrm{d}\theta\,\mathrm{d}|\boldsymbol{\xi}| = \frac{\pi c_0\delta^4 s_0^2}{4} \tag{A.7}$$

The equivalence principle asserts that the strain energy density calculated from continuum mechanics and peridynamics should be equal. Therefore, comparing Eq. (A.2) with Eqs. (A.3) ~ (A.7) leads to:

$$W^{\mathrm{CM}} = W^{\mathrm{PD}} \tag{A.8}$$

The expressions of c_0 corresponding to different forms of $g(\boldsymbol{\xi})$ can be derived as follows:

$$c_0 = \begin{cases} \dfrac{3}{\left(12 - \dfrac{32}{\mathrm{e}}\right)} \dfrac{E}{(1-2\nu)\delta^4\pi}, & \text{Exponential VBF} \\ \dfrac{3}{\left(1 - \dfrac{2}{\mathrm{e}}\right)} \dfrac{E}{(1-2\nu)\delta^4\pi}, & \text{Gaussian VBF} \\ \dfrac{36E}{(1-2\nu)\delta^4\pi}, & \text{Parabolic VBF} \\ \dfrac{3\pi^4}{4(\pi^3 - 24\pi + 48)} \dfrac{E}{(1-2\nu)\pi\delta^4}, & \text{Cosinoidal VBF} \\ \dfrac{6E}{(1-2\nu)\delta^4\pi}, & \text{Constant VBF} \end{cases} \tag{A.9}$$

The results of different VBF forms are summarised in Table 1.

References

Augarde, C.E., Lee, S.J., Loukidis, D., 2021. Numerical modelling of large deformation problems in geotechnical engineering: A state-of-the-art review. Soils Found. 61(6), 1718-1735. https://doi.org/10.1016/j.sandf.2021.08.007

Azéma, E., Radjai, F., Dubois, F., 2013. Packings of irregular polyhedral particles: Strength, structure, and effects of angularity. Phys. Rev. E 87(6), 062203. https://doi.org/10.1103/PhysRevE.87.062203

Bažant,, Z.P., Planas, J., 1998. Fracture and size effect in concrete and other quasibrittle materials. New York: Routledge.

Bie, Y., Ren, H., Rabczuk, T., Bui, T.Q., Wei, Y., 2024a. The fully coupled thermo-mechanical dual-horizon peridynamic correspondence damage model for homogeneous and heterogeneous materials. Comput. Methods Appl. Mech. Eng. 420, 116730. https://doi.org/10.1016/j.cma.2023.116730

Bie, Y., Ren, H., Bui, T.Q., Madenci, E., Rabczuk, T., Wei, Y., 2024b. Dual-horizon peridynamics modeling of coupled chemo-mechanical-damage for interface oxidation-induced cracking in thermal barrier coatings. Comput. Methods Appl. Mech. Eng. 430, 117225. https://doi.org/10.1016/j.cma.2024.117225

Blanc, N., Frank, X., Radjai, F., Mayer-Laigle, C., Delenne, J.Y., 2021. Breakage of flawed particles by peridynamic simulations. Comput. Part. Mech. 8, 1019-1031. https://doi.org/10.1007/s40571-021-00390-5

Bobaru, F., Foster, J.T., Geubelle, P.H., Silling, S.A., 2016. Handbook of peridynamic modeling. New York: CRC Press.

Bobaru. F., Zhang. G., 2015. Why do cracks branch? A peridynamic investigation of dynamic brittle fracture. Int. J. Fract. 196(1): 59-98. http://dx.doi.org/10.1007/s10704-015-0056-8

Bui, H.H., Nguyen, G.D., 2021. Smoothed particle hydrodynamics (SPH) and its applications in geomechanics: From solid fracture to granular behaviour and multiphase flows in porous media. Comput. Geotech. 138, 104315. https://doi.org/10.1016/j.compgeo.2021.104315

Buscarnera, G., Einav, I., 2021. The mechanics of brittle granular materials with coevolving grain size and shape. Proc. R. Soc. A 477(2249), 20201005. https://doi.org/10.1098/rspa.2020.1005

Chen, W., Wang, L., Tan, X., et al., 2021. State-of-the-art and development tendency of the underground engineering stability of fractured rock mass. Chinese J. Rock Mech. Eng. 40(10), 1945-1961. http://rockmech.whrsm.ac.cn/EN/Y2021/V40/I10/1945

Chen, Y., Yang, Y., Liu, Y., 2023. Large deformation and crack propagation analyses of hydrogel by peridynamics. Eng. Fract. Mech. 284, 109261. https://doi.org/10.1016/j.engfracmech.2023.109261

Chung, Y.L., Chiang, Y.C., 1996. Dynamic micro-structural finite element method for granular structures. Eng. Fract. Mech. 53(4), 593-606. https://doi.org/10.1016/0013-7944(95)00128-X

de Bono, J.P., McDowell, G.R., 2020. On the packing and crushing of granular materials. Int. J. Solids Struct. 187, 133-140. https://doi.org/10.1016/j.ijsolstr.2018.07.011

de Gennes, P.G., 1998. Reflections on the mechanics of granular matter. Physica A 261(3-4), 267-293. https://doi.org/10.1016/S0378-4371(98)00438-5

Diehl, P., Prudhomme, S., Lévesque, M., 2019. A review of benchmark experiments for the validation of peridynamics models. J. Peridyn. Nonlocal Model. 1, 14-35. https://doi.org/10.1007/s42102-018-0004-x

Einav, I., 2007a. Breakage mechanics-Part I: Theory. J. Mech. Phys. Solids 55(6), 1274-1297. https://doi.org/10.1016/j.jmps.2006.11.003

Einav, I., 2007b. Breakage mechanics-Part II: Modelling granular materials. J. Mech. Phys. Solids 55(6), 1298-1320. https://doi.org/10.1016/j.jmps.2006.11.004

Hall, S.A., Wright, J., 2015. Three-dimensional experimental granular mechanics. Géotechnique Lett. 5(4), 236-242. https://doi.org/10.1680/jgele.15.00094

Henkes, S., Chakraborty, B., 2009. Statistical mechanics framework for static granular matter. Phys. Rev. E,79(6), 061301. https://doi.org/10.1103/PhysRevE.79.061301

Huang, D., Lu, G., Wang, C., Qiao, P., 2015a. An extended peridynamic approach for deformation and fracture analysis. Eng. Fract. Mech. 141, 196-211. https://doi.org/10.1016/j.engfracmech.2015.04.036

Huang, Y., Yang, Z., Ren, W., Liu, G., Zhang, C., 2015b. 3D meso-scale fracture modelling and validation of concrete based on in-situ X-ray Computed Tomography images using damage plasticity model. Int. J. Solids Struct. 67, 340-352. https://doi.org/10.1016/j.ijsolstr.2015.05.002

Huang, Y., Natarajan, S., Zhang, H., Guo, F.Q., Xu, S.L., Zeng, C., Zheng, Z.S., 2023. A CT image-driven computational framework for investigating complex 3D fracture in mesoscale concrete. Cem. Concr. Compos. 143, 105270. https://doi.org/10.1016/j.cemconcomp.2023.105270

Jin, Y.F., Yin, Z.Y., Li, J., Dai, J.G., 2021. A novel implicit coupled hydro-mechanical SPFEM approach for modelling of delayed failure of cut slope in soft sensitive clay. Comput. Geotech. 140, 104474. https://doi.org/10.1016/j.compgeo.2021.104474

Kilic, B., Madenci, E., 2009. Structural stability and failure analysis using peridynamic theory. Int. J. Non-Linear Mech. 44(8), 845-854. https://doi.org/10.1016/j.ijnonlinmec.2009.05.007

Konrad, J.M., Salami, Y., 2018. Particle breakage in granular materials-a conceptual framework. Can. Geotech. J. 55(5), 710-719. https://doi.org/10.1139/cgj-2017-0224

Li, S., Jin, Y., Lu, H., Sun, P., Huang, X., Chen, Z., 2021. Wave dispersion and quantitative accuracy analysis of bond-based peridynamic models with different attenuation functions. Comput. Mater. Sci. 197, 110667. https://doi.org/10.1016/j.commatsci.2021.110667

Li, X., Wang, Z., Liang, Y., Duan, Q., 2016. Mixed FEM-crushable DEM nested scheme in second-order computational homogenization for granular materials. Int. J. Geomech. 16(5), C4016004. https://doi.org/10.1061/(ASCE)GM.1943-5622.0000627

Li, Z., Liu, B., Han, D., Xie, Y., Zhao, Y., 2024. Study on the influence of microcracks of coarse aggregate with specific particle size on crushing strength. Comput. Part. Mech. 11(2), 705-719. https://doi.org/10.1007/s40571-023-00648-0

Liang, W., He, K.Y., Jin, Y.F., Yin, Z.Y., 2024. A gradient-smoothed material point method for reducing cell crossing noise in large deformation problems. Comput. Geotech. 169, 106169. https://doi.org/10.1016/j.compgeo.2024.106169

Liu, Y., Wang, L., Hong, Y., Zhao, J., Yin, Z.Y., 2020. A coupled CFD-DEM investigation of suffusion of gap graded soil:

Coupling effect of confining pressure and fines content. Int. J. Numer. Anal. Methods Geomech. 44(18), 2473-2500. https://doi.org/10.1002/nag.3151

Lobo-Guerrero, S., Vallejo, L.E., 2005. Crushing a weak granular material: experimental numerical analyses. Géotechnique, 55(3), 245-249. https://doi.org/10.1680/geot.2005.55.3.245

Longo, A., Pastor, M., Sanavia, L., Manzanal, D., Martin Stickle, M., Lin, C., Yague, A., Tayyebi, S.M., 2019. A depth average SPH model including rheology and crushing for rock avalanches. Int. J. Numer. Anal. Methods Geomech. 43(5), 833-857. https://doi.org/10.1002/nag.2912

Lu, W., Oterkus, S., Oterkus, E., Zhang, D., 2021. Modelling of cracks with frictional contact based on peridynamics. Theor. Appl. Fract. Mech. 116, 103082. https://doi.org/10.1016/j.tafmec.2021.103082

Ma, G., Zhou, W., Chang, X.L., Chen, M.X., 2016. A hybrid approach for modeling of breakable granular materials using combined finite-discrete element method. Granular Matter 18, 1-17. https://doi.org/10.1007/s10035-016-0615-3

Madenci, E., Oterkus, E., 2013. Peridynamic theory. In: Peridynamic theory and its applications. New York: Springer. http://dx.doi.org/10.1007/978-1-4614-8465-3

Malvern, L.E., 1969. Introduction to the Mechanics of a Continuous Medium. Hemel Hempstead, Hertfordshire, England.

Mendes, N., Chhay, M., Berger, J., Dutykh, D., 2019. Explicit schemes with improved CFL condition. In: Numerical methods for diffusion phenomena in building physics. Cham: Springer.

Mesri, G., Vardhanabhuti, B., 2009. Compression of granular materials. Can. Geotech. J. 46(4), 369-392. https://doi.org/10.1139/T08-123

Neto, A.G., 2023. Framework for automatic contact detection in a multibody system. Comput. Methods Appl. Mech. Eng. 403, 115703. https://doi.org/10.1016/j.cma.2022.115703

Ogata, S., Yasuhara, H., 2023. Numerical simulations for describing generation of excavation damaged zone: Important case study at Horonobe underground research laboratory. Rock Mech Bull. 2(3), 100063. https://doi.org/10.1016/j.rockmb.2023.100063

Parks, M.L., Lehoucq, R.B., Plimpton, S.J., Silling, S.A., 2008. Implementing peridynamics within a molecular dynamics code. Comput. Phys. Comm. 179(11), 777-783. https://doi.org/10.1016/j.cpc.2008.06.011

Pöschel, T., Schwager, T., 2005. Computational granular dynamics: models and algorithms. Berlin: Springer-Verlag.

Ren, H.L., Zhuang, X.Y., Anitescu, C., Rabczuk, T., 2019. An explicit phase field method for brittle dynamic fracture. Comput. Struct.217, 45-56. http://dx.doi.org/10.1016/j.compstruc.2019.03.005

Rui, S., Guo, Z., Si, T., Li, Y., 2020. Effect of particle shape on the liquefaction resistance of calcareous sands. Soil Dyn. Earthquake Eng. 137, 106302. https://doi.org/10.1016/j.soildyn.2020.106302

Sac-Morane, A., Veveakis, M., Rattez, H., 2024. A Phase-Field Discrete Element Method to study chemo-mechanical coupling in granular materials. Comput. Methods Appl. Mech. Eng. 424, 116900. https://doi.org/10.1016/j.cma.2024.116900

Silling, S.A., 2000. Reformulation of elasticity theory for discontinuities and long-range forces. J. Mech. Phys. Solids 48(1), 175-209. https://doi.org/10.1016/S0022-5096(99)00029-0

Silling, S.A., Askari, E., 2005. A meshfree method based on the peridynamic model of solid mechanics. Comput. Struct. 83(17-18), 1526-1535. https://doi.org/10.1016/j.compstruc.2004.11.026

Silling, S.A., Epton, M., Weckner, O., Xu, J., Askari, E., 2007. Peridynamic states and constitutive modeling. J. Elast. 88, 151-184. http://dx.doi.org/10.1007/s10659-007-9125-1

Silling, S.A., Lehoucq, R.B., 2010. Peridynamic theory of solid mechanics. Adv. Appl. Mech. 44, 73-168. http://dx.doi.org/10.1016/S0065-2156(10)44002-8

Smith, M., 2009. ABAQUS/Standard User's Manual Version 6.9. Dassault Systèmes Simulia Corp.

Tan, X., Chen, W., Wang, L., Yang, J., Tan, X.J., 2021. Settlement behaviors investigation for underwater tunnel considering the impacts of fractured medium and water pressure. Mar. Geores. Geotechnol. 39, 639-648. https://doi.org/10.1080/1064119X.2020.1737279

Tang, Y., Qiu Z., Deng W., 2022. Research of crushing characteristics and strength characteristics considering single particle crushing mode. Water Resour. Hydropower Eng. 53(7), 169-179. https://doi.org/10.13928/j.cnki.wrahe.2022.07.016

Turner, A.K., Sharma, A., Penumadu, D., Herbold, E.B., 2019. Finite element analyses of single particle crushing tests incorporating computed tomography imaging and damage mechanics. Comput. Geotech. 115, 103158. https://doi.org/10.1016/j.compgeo.2019.103158

Walayat, K., Haeri, S., Iqbal, I., Zhang, Y., 2023. Hybrid PD-DEM approach for modeling surface erosion by particles impact. Comput. Part. Mech. 10, 1895-1911. https://doi.org/10.1007/s40571-023-00596-9

Wan, J., Chen, Z., Chu, X., Liu, H., 2020. Dependency of single-particle crushing patterns on discretization using peridynamics. Powder Technol. 366, 689-700. https://doi.org/10.1016/j.powtec.2020.03.021

Wang, L., Vuik, C., Hajibeygi, H., 2022. A stabilized mixed-FE scheme for frictional contact and shear failure analyses in deformable fractured media. Eng. Fract. Mech. 267, 108427. https://doi.org/10.1016/j.engfracmech.2022.108427

Wang, L., Yin, Z.Y., Chen, W., 2023. Peridynamic modelling of dynamic damage and fragmentation of cracked solids during impact contact. Eng. Fract. Mech. 295, 109784. https://doi.org/10.1016/j.engfracmech.2023.109784

Wang, L., Yin, Z.Y., Chen, W., 2024a. Characteristics of crack growth in brittle solids with the effects of material heterogeneity and multi-crack interaction. Int. J. Fract. 246, 77-99. https://doi.org/10.1007/s10704-024-00771-w

Wang, L., Yin, Z.Y., 2024b. Modelling finite deformation and progressive failure of hyperelastic solid with implicit BA-NOSB-PD. Comput. Methods Appl. Mech. Eng. 431, 117260. https://doi.org/10.1016/j.cma.2024.117260

Wang, L., Yin, Z.Y., 2025. A unified bond-based peridynamic model with insights into high-frequency elastodynamic problems in geotechnical and structural engineering. Int. J. Numer. Anal. Methods Geomech. 1-22. https://doi.org/10.1002/nag.70062

Wang, P., Yin, Z.Y., 2022. Effect of particle breakage on the behavior of soil-structure interface under constant normal stiffness condition with DEM. Comput. Geotech. 147, 104766. https://doi.org/10.1016/j.compgeo.2022.104766

Wang, T., Wang, P., Yin, Z. Y., Zhang, F., Xu, C., 2025. DEM-DFM modeling suffusion of granular soils under triaxial compression. Int. J. Geomech. 25(2), 04024352. https://doi.org/10.1061/IJGNAI.GMENG-10162

Wei, D., Zhao, B., Dias-da-Costa, D., Gan, Y., 2019. An FDEM study of particle breakage under rotational point loading. Eng. Fract. Mech. 212, 221-237. https://doi.org/10.1016/j.engfracmech.2019.03.036

Wong, L.N.Y., Cui, X., 2023. Simulation of 3D fracture propagation under I-II-III mixed-mode loading. Rock Mech Bull. 2(4), 100082. https://doi.org/10.1016/j.rockmb.2023.100082

Wriggers, P., 2006. Computational contact mechanics (2nd edition). Berlin: Springer-Verlag.

Yin, Z.Y., Jin, Z., Kotronis, P., Wu, Z.X., 2018. Novel SPH SIMSAND-based approach for modeling of granular collapse. Int. J. Geomech. 18(11), 04018156. https://doi.org/10.1061/(ASCE)GM.1943-5622.000125

Zar, A., Hussain, Z., Akbar, M., Rabczuk, T., Lin, Z., Li, S., Ahmed, B., 2024. Towards vibration-based damage detection of civil engineering structures: overview, challenges, and future prospects. Int. J. Mech. Mater. Des. 20(3), 591-662. https://doi.org/10.1007/s10999-023-09692-3

Zhang, H., Zhang, X., Liu, Y., 2022. A peridynamic model for contact problems involving fracture. Eng. Fract. Mech. 267, 108436. http://dx.doi.org/10.1016/j.engfracmech.2022.108436

Zhang, Z., Gu, H.，Wang, H.，Tang, L., Liu, X., Qi, H., 2020. Numerical simulation of internal crack propagation in rocks under semi-circle bending. Water Resour. Hydropower Eng. 51(4), 193-202. http://dx.doi.org/10.13928/j.cnki.wrahe.2020.04.023

Zhao, B., Wang, J., Coop, M.R., Viggiani, G., Jiang, M., 2015. An investigation of single sand particle fracture using X-ray micro-tomography. Géotechnique, 65(8), 625-641. https://doi.org/10.1680/geot.4.P.157

Zhao, J., Zhao, S., Luding, S., 2023. The role of particle shape in computational modelling of granular matter. Nat. Rev. Phys. 5(9), 505-525. https://doi.org/10.1038/s42254-023-00617-9

Zhu, F., Zhao, J., 2019. A peridynamic investigation on crushing of sand particles. Géotechnique, 69(6), 526-540. https://doi.org/10.1680/jgeot.17.P.274